International Journal of Extreme Manufacturing

Alloy design for laser powder bed fusion additive manufacturing: a critical review

To cite this article before publication: Zhuangzhuang Liu *et al* 2023 *Int. J. Extrem. Manuf.* in press https://doi.org/10.1088/2631-7990/ad1657

Alloy design for laser powder bed fusion additive manufacturing: a critical review

Journal:	*International Journal of Extreme Manufacturing*
Manuscript ID	IJEM-111114.R1
Manuscript Type:	Topical Review
Keywords:	Additive manufacturing, Laser powder bed fusion, Alloy design

Alloy design for laser powder bed fusion additive manufacturing: a critical review

Zhuangzhuang Liu [1, 2, 3], Qihang Zhou [1], Xiaokang Liang [4], Xiebin Wang [5], Guichuan Li [6], Kim Vanmeensel [6], Jianxin Xie [1, 2, 3, *]

[1] Key Laboratory for Advanced Materials Processing (MOE), Institute for Advanced Materials and Technology, University of Science and Technology Beijing, Beijing 100083, China

[2] Beijing Advanced Innovation Center for Materials Genome Engineering, University of Science and Technology Beijing, Beijing 100083, China

[3] Beijing Laboratory of Metallic Materials and Processing for Modern Transportation, Institute for Advanced Materials and Technology, University of Science and Technology Beijing, Beijing 100083, China

[4] Capital Aerospace Machinery Corporation Limited, Beijing 100076, China

[5] Key Laboratory for Liquid-Solid Structural Evolution and Processing of Materials (Ministry of Education), Shandong University, Jingshi Road 17923, Jinan 250061, China.

[6] Department of Materials Engineering, KU Leuven, Leuven, 3001, Belgium

* Corresponding author and E-mail: Jianxin Xie (jxxie@mater.ustb.edu.cn)

1. Abstract

Metal additive manufacturing (AM) has been extensively studied in recent decades. Despite the significant progress achieved in manufacturing complex shapes and structures, challenges such as severe cracking when using existing alloys for laser powder bed fusion (L-PBF) AM persisted. These challenges arise because commercial alloys are primarily designed for conventional casting or forging processes, overlooking the fast cooling rates, steep temperature gradients, and multiple thermal cycles of L-PBF. To address this, there is an urgent need to develop novel alloys specifically tailored for L-PBF technologies. This review provides a comprehensive summary of the strategies employed in alloy design for L-PBF. It aims to guide future research on designing novel alloys dedicated to L-PBF instead of adapting the existing alloys for L-PBF. The review begins by discussing the features of L-PBF processes, focusing on rapid solidification and intrinsic heat treatment. Next, the printability of the four main existing alloys (Fe-, Ni-, Al-, and Ti-based alloys) is critically assessed, with a comparison to their conventional weldability. It was found that the weldability criteria are not always applicable in estimating printability. Furthermore, the review presents recent advances in alloy development and associated strategies, categorizing them into crack mitigation-oriented, microstructure manipulation-oriented, and machine learning-assisted approaches. Lastly, an outlook and suggestions are given to highlight the issues that need to be addressed in future work.

Keywords: laser powder bed fusion, alloy design, printability, crack mitigation

2. Introduction

Additive Manufacturing (AM), building objects layer by layer directly from three-dimensional data [1], has been regarded as a revolutionary manufacturing technology since it was born in the 1980s [2]. The early studies primarily focused on polymers and AM was used for rapid prototyping applications. Later on, with the introduction of selective laser melting (SLM, also termed as laser powder bed fusion, L-PBF) in the 1990s [3], the AM technology has been widely used for the production of complex metal parts. Nowadays, the AM technology gained recognition for end-use part production, particularly in aerospace, automotive, and medical industries [4-6].

In contrast to traditional 'subtractive' manufacturing, AM offers notable advantages. AM allows for complex geometries, including internal cavities, undercuts, and intricate lattice structures, without the constraints of traditional manufacturing methods. AM also enables quick iterations in the design process, reducing time and costs associated with tooling. Additionally, parts can be designed with specific material properties and optimized for their intended function, leading to lightweight and efficient designs [7-10].

Despite notable achievements in manufacturing complex shapes and structures using AM [11-14], the availability of printable metals that are crack-free in the as-built state is still limited. The presence of defects such as cracks and pores significantly compromises the mechanical properties, as the alloys were initially designed for wrought or casting without considering the unique characteristics of the AM process. Laser powder bed fusion (L-PBF) additive manufacturing involves high cooling rates, steep temperature gradients, and numerous thermal cycles[15, 16]. The compositions of many existing alloys are not well-suited for these characteristics, leading to cracking when directly applied to L-PBF. For instance, while boron is added to nickel-based superalloys in casting to enhance grain boundary cohesion and improve creep properties [17], its addition in L-PBF is detrimental, causing hot cracking due to reduced solidus temperature and the formation of a stabilized liquid film at lower temperatures [18]. Therefore, a novel alloy design approach is necessary, taking into account the processability during L-PBF.

Metal additive manufacturing has been extensively reviewed by various research groups from different perspectives, for instance the microstructure [19, 20], processing [21, 22], numerical modelling [23-25], mechanical properties [21, 26, 27], and post-treatments [28-30]. The alloy development has also been reviewed, including Ti-based[31-35], Al-based[20, 36], Ni-based[37, 38], Fe-based[2, 39], and Mg-based alloys[40, 41]. However, most of the work focuses on adapting existing alloys to the L-PBF process, rather than developing specific alloys dedicated to L-PBF. Furthermore, there is a lack of analysis on the correlation between elements and the printability of an alloy system in existing reviews. Additionally, less attention has been paid to comparing the weldability and printability of the existing alloys. Therefore, in this work, we first analyze the differences between conventional casting/welding processes and L-PBF process. Subsequently, the weldability and printability of commonly used alloy systems are analyzed, i.e., Fe-based, Ni-based, Al-based, and Ti-based, assessing the validity of using convention weldability to predict printability and identifying problems when using existing alloys in L-PBF. Subsequently, strategies used in alloy design for L-PBF are summarized and categorized into crack mitigation-oriented, microstructure manipulation-oriented, and machine learning-assisted approaches. At last, the current development of alloy design for L-PBF is summarized, and suggestions for future work are provided. The purpose of this review work is to provide guidance and new insights for designing novel alloys specifically tailored for L-PBF.

3. Laser powder bed fusion

The prevalent metal additive manufacturing technologies primarily include powder bed fusion (PBF) and directed energy deposition (DED), as shown in **Figure 1**. The metal powder in PBF is spread uniformly over a build platform, and each layer is selectively melted according to the 3D model. In DED, both metal powders and wires can be used to precisely deposit on a substrate or previously deposited layers through a nozzle or feedstock mechanism. In general, PBF processes typically offer higher resolution and accuracy, resulting in parts with fine details and intricate geometries, comparing to DED. However, DED technologies offer greater deposition freedom than PBF, as they can be used to fabricate and repair parts in a more flexible manner, enabling large-scale production.

The PBF can be further categorized into laser powder bed fusion (L-PBF) and electron powder bed fusion (E-PBF) based on the types of heat sources employed, as shown in **Figure 1**. The laser beam used in L-PBF is a coherent beam of light with specific wavelengths, typically in the infrared range. The electron beam used in E-PBF consists of accelerated electrons. It has a larger interaction volume and can penetrate deeper into the material, thus creating larger melt pools than laser. Furthermore, the build chamber during E-PBF can be heated to a much higher temperature, e.g., 1 000℃, while most of the commercial L-PBF equipment can only preheat the baseplate to 200℃. L-PBF typically exhibits high cooling rates due to the localized melting and rapid solidification of the metal powder. The localized melting and solidification result in steep thermal gradients between the molten and solidified regions. Therefore, L-PBF can produce fine-grained microstructures. In this review, we primarily focus on alloy design for the L-PBF technology, but will also cite multiple works on E-PBF or DED as a comparison or reference to inspire future alloy design work for L-PBF.

As shown in **Figure 1**, during L-PBF, a thin layer of metal powder, typically around 20 ~ 100 micrometers thick, is evenly spread across a metal plate. A laser beam is precisely guided across the powder bed in a pattern defined by the 3D model. As the laser beam scans the powder bed, metallic powders absorb laser light and convert it into heat energy. It should be noted that part of the laser energy can reflect off the powder's surface due to its high reflectivity. When the temperature reaches or exceeds the powder's melting point, the particles start to melt, forming a localized molten pool and then cooling down rapidly. After each layer is melted and solidified, the build platform is lowered by a layer thickness. A new layer of metal powder is then spread across the previously printed layer. The process is repeated, building the object layer by layer until it is fully formed. Metal powders used in L-PBF should have a controlled particle size and shape, as well as good flowability and homogeneity. These properties are crucial for uniform powder spreading and influence the laser-powder interaction and energy absorption, impacting the final microstructure and properties of the printed object [42].

Comparing to conventional casting, metallic parts undergo much higher cooling rates ($10^3 \sim 10^8$ °C·s^{-1})[43] and heating rates during L-PBF. Due to the layer-wise printing nature, the solidified section experiences multiple thermal cycles, which is termed as intrinsic heat treatment (IHT). The IHT generates substantial internal thermal stresses and dislocations within the solidified part, playing a significant role in the part properties. This section provides an overview of the key characteristics of L-PBF, highlighting the associated advantages and challenges.

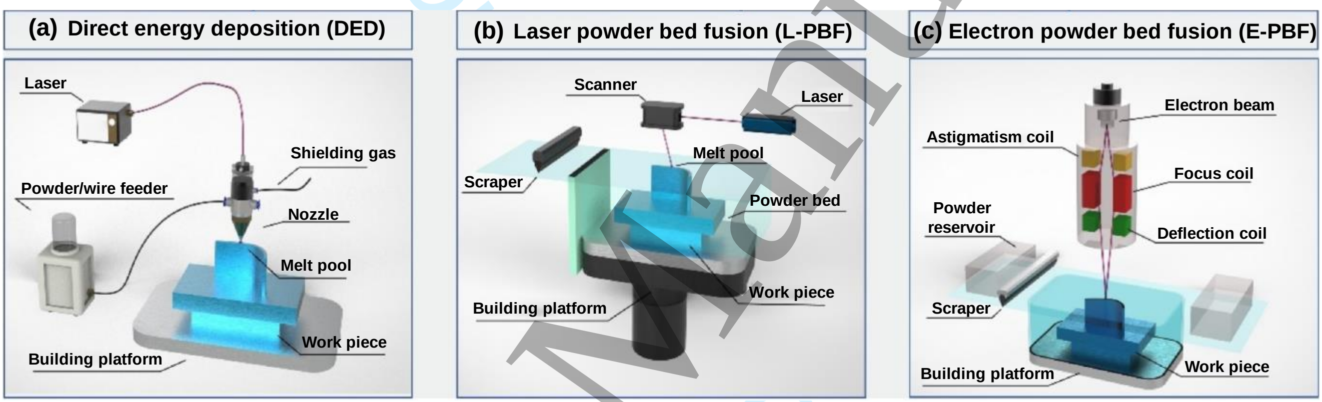

Figure 1. Three widely used metal additive manufacturing processes. **(a)** Direct energy deposition (DED). **(b)** Laser powder bed fusion (L-PBF). **(c)** Electron powder bed fusion (E-PBF)[44].

3.1 Features

In laser powder bed fusion, metallic parts undergo complex thermal cycles [45, 46]. Initially, the powders interact with the laser beam and are melted at a fast heating rate. As the heat source moves away, the melt pool cools down rapidly and is solidified. The as-solidified parts then experience additional thermal cycles arising from the melting of subsequent tracks and neighboring layers.

(1) Rapid solidification

During L-PBF, the layer-by-layer scanning of high-power laser is essentially a non-equilibrium process [47]. a large amount of heat input will be applied to the metal powder, and the powder temperature can exceed 2 000°C (**Figure 2**(c)) [48]. This results in a steep temperature gradient from the center of the melt pool to its boundary. Upon laser removal, the material rapidly solidifies at a cooling rate of roughly 10^5 °C·s^{-1}[49].

As a comparison, the cooling rate in conventional casting is approximately 0.5 °C·s^{-1} [43]. Consequently, the additively manufactured microstructure is one or two orders of magnitude smaller than the as-cast materials [50]. The repeated ultrafast heating and cooling cycles during L-PBF also gives rise to a higher dislocation density comparing to their cast counterparts [12]. Moreover, the additively manufactured microstructure exhibits supersaturated solid solution with micro-segregation along dendrite arms [51] as a result of the high cooling rate. Furthermore, the steep temperature gradient leads to an intense Marangoni flow in the melts [52], affecting the chemical uniformity within the melt pool [53].

***(2)* Intrinsic heat treatment**

In casting, materials typically undergo a single heating-cooling cycle. In contrast, in laser powder bed fusion, the powders are melted and cooled first, and the resulting solidified part can undergo multiple cycles of reheating or even remelting as the laser scans adjacent hatches or subsequent layers. The intricate physical process and thermal history result in high thermal residual stresses, heterogeneous metastable microstructures, and non-equilibrium compositions or phase distributions within the final part [20, 54, 55] (**Figure 2** (b) and (d)) [20, 48].

For instance, the intrinsic heat treatment during L-PBF enables the element partitioning at grain boundaries and potential precipitate formation. However, this unique feature of L-PBF can also bring manufacturing challenges for some specific alloys. The precipitates at grain boundaries, dendritic boundaries, and melt pool boundaries can cause boundary liquation or local stress/strain concentration due to the layer-by-layer scanning pattern during L-PBF. For instance, micro-segregation of Nb and Ti in L-PBF Inconel 718 alloy leads to the formation of brittle Laves and δ phases, increasing the crack susceptibility. Homogenization heat treatment is thus generally employed to equalize element distribution (e.g., Ti and Nb in Inconel 718) and potentially dissolve harmful phases (e.g., Laves and δ phases) present in the as-printed alloys [54]. Another typical characteristic of L-PBF is the high internal thermal stress, which is accumulated during thermal cycling. The thermal stress could cause cracks and geometric distortions of the components during L-PBF (**Figure 2**(a)) [56]. Furthermore, the L-PBF-processed alloys are inherently anisotropic [57] as a result of epitaxial grain growth, which is prevalent in laser powder bed fusion. Large columnar grain is known for the capillary effect and poor strain accommodation capability [48]. As a result of the microstructural non-uniformities [54], the mechanical response depends on the loading direction relative to the build direction, leading to anisotropic mechanical properties.

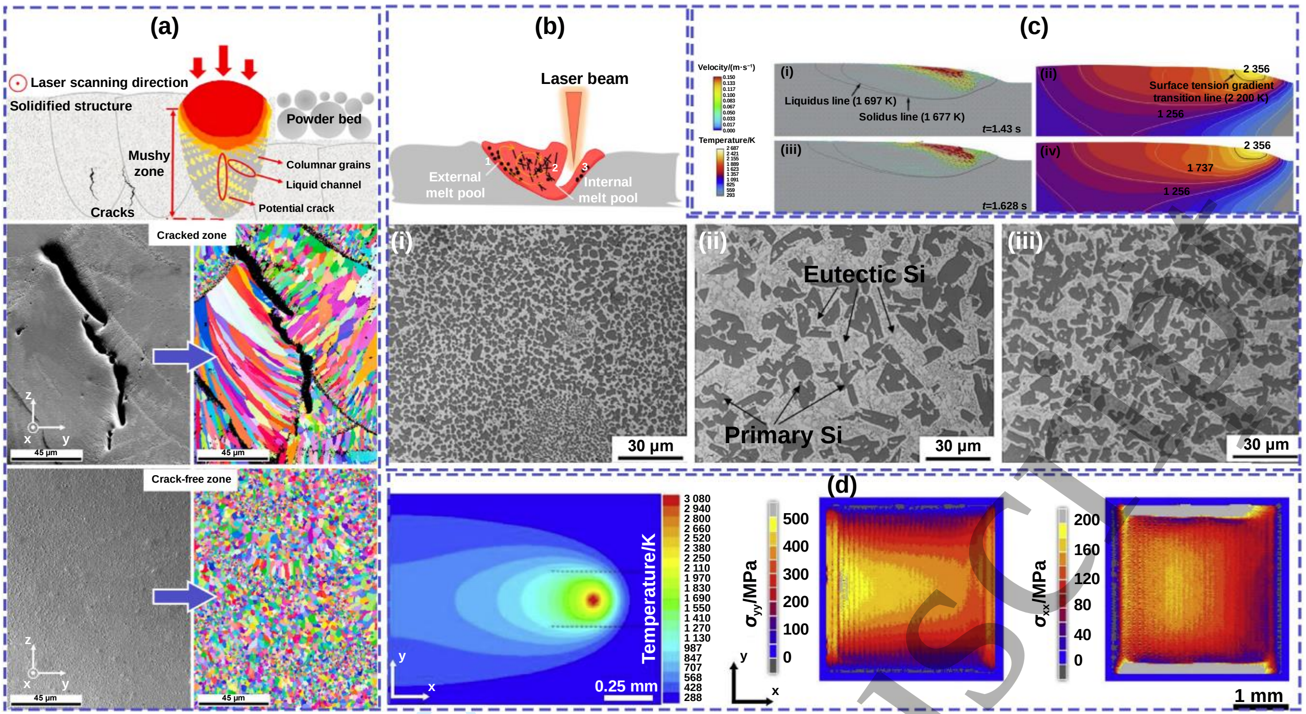

Figure 2. Effects of complex physical processes and thermal history of LPBF on microstructure, phase and stress distribution. **(a)** Schematic diagram of cracking in Al-Cu-Mg alloy and the microstructure of cracked and uncracked regions [56]; **(b)** L-PBF processed over-eutectic Al-50Si alloy. Complex thermal physical processes generate non-equilibrium phase distribution [20]; **(c)** longitudinal sections of mass flow velocity and temperature distribution of depositing single track at different times [48]; **(d)** anisotropic stress field in each layer under the influence of multiple anisotropic beam paths[55].

3.2 Defects

In L-PBF, the quality of printed parts is influenced by multiple factors such as metallic powders (flowability, particle size distribution, et al.), laser beam (beam diameter, beam intensity profile, et al.), and scanning strategies (hatch manner, inter-layer rotational angel, et al.). The defects occurred in additively manufactured alloys primarily include gas pores, keyhole, lack-of-fusion pores, and cracks, as shown in **Figure 3** [58].

The **gas pores** in the as-built microstructure typically originate from either the gas pores in the feedstock powders or the shielding gas entrapped during intensive melt pool flow in L-PBF. The gas pores primarily occur at occasions when there is insufficient time duration for the gas bubble to escape from the melt pool prior to solidification.

Lack-of-fusion (LoF) pores, as the name implies, are due to the insufficient melting of powders and are evident to occur at low energy input. The un-completely melted powders constantly leave a triangle space between two neighboring hatches. Due to the sharp appearance, the LoF is detrimental to the mechanical behavior.

In contrast to LoF, which occurs at insufficient energy input, the **keyhole** defect is observed at excessive heat input. During L-PBF, the high-energy laser beam interacts with the powder beds. The powders at the surface boil and form a strong steam jet as a result of local heating. The steam jet then pushes the melt down due to the recoil pressure, forming a vapor depression (**Figure 3**), which is known as keyhole [59].

The keyhole, gas porosity, and LoF defects (**Figure 4** (a)-(c)) can be minimized or completely removed in the as-built parts by optimizing the scanning parameters or applying hot isostatic pressing (HIP) treatment. However, cracks, which are intolerant in most of the LPBF-processed parts, are still intractable for the majority of the existing metals and hinder the application of L-PBF in the industry.

Depending on their origins, cracks occurred during L-PBF are categorized as hot cracking and solid-state cracking [60]. Hot cracking includes solidification cracking and liquation cracking. Solid-state cracking involves strain-age cracking and ductility-dip cracking.

Solidification cracking, also termed as hot tearing during welding, is believed to occur at the last stage of solidification [61]. Due to the rapid cooling, solute atoms are enriched in-between adjacent dendrites, reducing the solidus of the residual liquid. The shrinkage strain caused by solidification and thermal contraction can pull apart the residual liquid. If the liquid is insufficient to backfill the inter-dendritic cavities, cracks form with clear dendritic characteristics [62] (**Figure 4** (d)-(f)). It is widely accepted that the semi-solid zone is prone to solidification cracking [63]. Therefore, narrowing the solidification temperature range results in a small slurry zone and a reduced hot cracking susceptibility.

Liquation cracking occurs when the low melting point phase present in a solidified part is liquefied again due to the reheating from the adjacent regions (**Figure 4** (g)-(i)) [64]. In conventional welding, the liquation cracking is observed at the heat affected zone. During L-PBF, the liquation cracking generally occurs near the melt pool boundaries, which is attributed to the segregation induced liquation under the effect of cyclic heat treatment [65]. The enrichment of solute, e.g., boron [18] in superalloys, at inter-dendritic region significantly reduces the local solidus temperature, promoting the formation of liquation cracking.

Strain-age cracking (SAC) is mostly observed in γ' strengthened nickel-based alloys (**Figure 4** (j)-(l)) [64]. The SAC cracking is attributed to the joint effect of γ' precipitation and the residual stresses during L-PBF. The γ' phase might precipitate during the layer-by-layer printing, leading to local stress concentration. The concentrated stress is superposed with the large thermal stress accumulated during L-PBF, leading to strain-age cracking.

The mechanism of **ductility-dip cracking (DDC)** has not yet been completely understood. The grain boundary inoperability at the intermediate temperature range was found to be one of the factors causing DDC [66-68]. It is found that the ability of grain boundary sliding is significantly reduced at tortuous grain boundaries or at grain boundaries where precipitates like γ' and carbides are present. The suppressed grain boundary sliding is beneficial for enhancing creep resistance, yet, it causes strain concentration and generates voids. The connection of these voids significantly lowers the ductility and eventually leads to ductility dip cracking (**Figure 4** (m)-(o)) [64].

Both processing parameters and alloy chemistry are found to have a significant impact on the cracking behavior. However, no consensus on the root cause of cracking has been reached yet. In general, the alloys with high solidification shrinkage (nickel-based superalloys) and thermal expansion coefficient (aluminum alloys) are susceptible to cracking during L-PBF [69]. Moreover, the refractory metals (e.g., tungsten, tantalum, and molybdenum) and metals with high laser reflectivity (e.g., pure copper) are less printable as they are difficult to melt [70]. The alloys with volatile elements (magnesium, zinc, etc.) are also challenging due to the server evaporation during L-PBF.

In the past, most of the work focused on the adaption of existing alloys to additive manufacturing process. However, the thermal circumstance, solidification process, the melt pool kinetics, etc. of L-PBF are distinct from those of the conventional processes. Only an integrated consideration of the alloy design and the unique features of L-PBF could lead to the synergistic advancement of new materials and processing technologies [71].

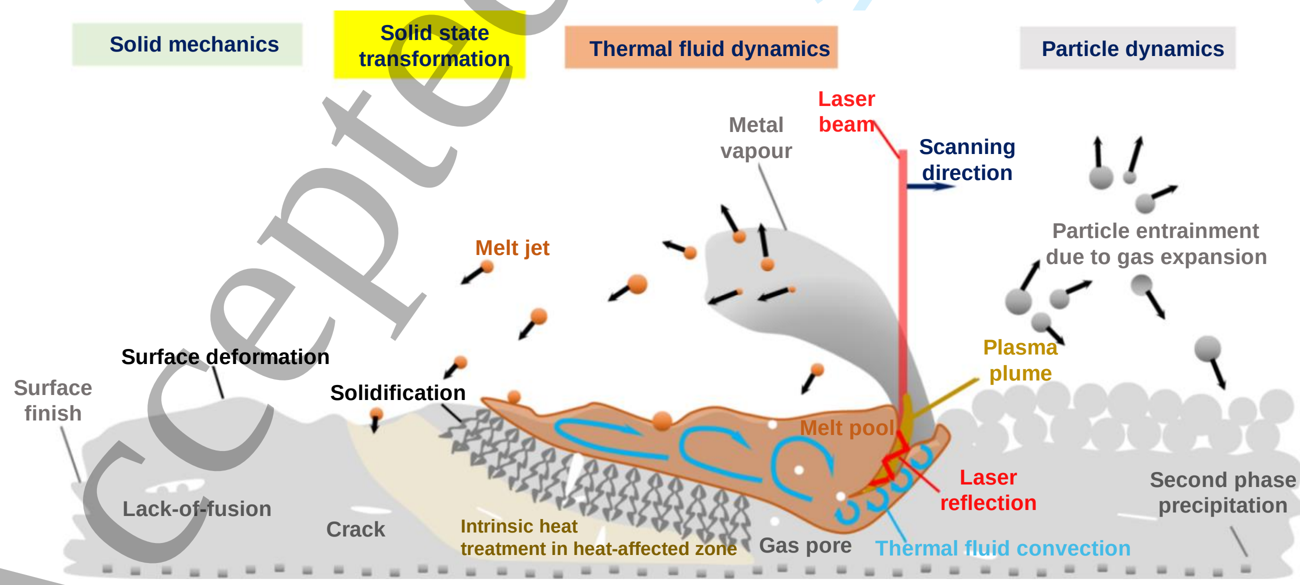

Figure 3. Complex metallurgical reactions during L-PBF [58].

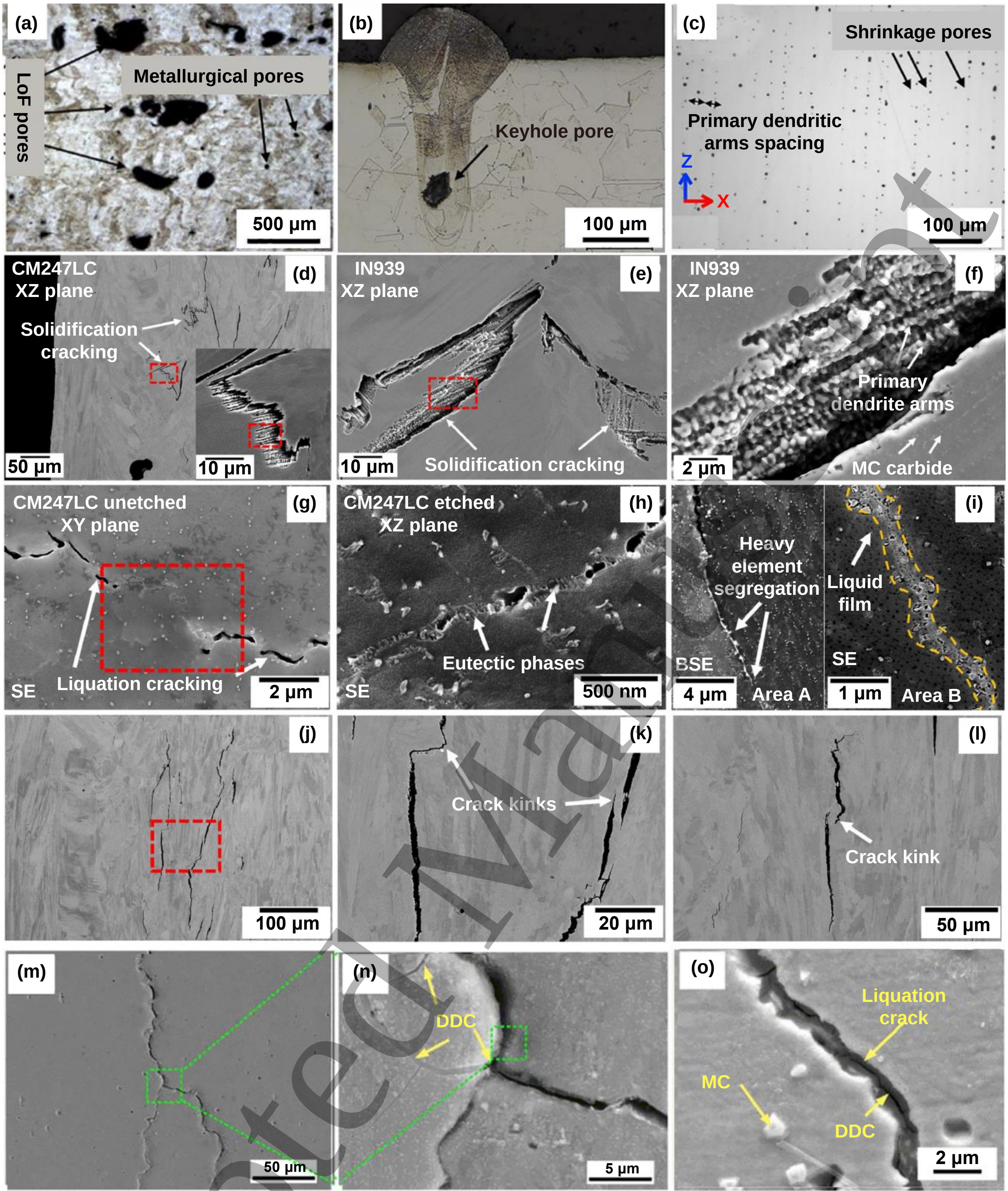

Figure 4. Common defects and their macroscopic and microscopic morphology: **(a)-(c)** porosity [64], **(d)-(f)** solidification cracking [72], **(g)-(i)** liquation cracking [72], and **(j)-(o)** solid-state cracking [64].

4. Printability of existing alloys

Defects, such as cracks in alloys, are intolerable for most of the applications. However, as mentioned in section 3.2, the existing alloys designed for conventional processes are not always suitable for the L-PBF process. As a result, defects such as pores and cracks can occur in alloys processed with L-PBF, and these defects are difficult to eliminate during the post-heat treatment. While hot isostatic pressing (HIP) can help to close internal cracks and pores, it is not capable of closing surface cracks. Moreover, HIP is both costly and time-consuming, which is less favorable for alloy processing. Hence, it is crucial to design alloys with higher crack resistance to prevent cracks from occurring in the first place.

Similar to weldability, which is widely used in the welding industry to characterize whether an alloy is easier to weld than others, printability is employed in the additive manufacturing industry. It is the term rating the ability of an alloy to be printed without defects, particularly cracks[15]. The printability of an alloy is generally determined by trial-and-error tests. In the literature, there are several mathematical and empirical models assessing the cracking vulnerability of alloys during L-PBF. Most of the models or equations were modified based on the understanding of welding or casting processes. However, it is worth mentioning that additive manufacturing, particularly L-PBF, has much steeper temperature gradients and higher cooling rates than welding and casting, leading to large deviation in microstructure and cracking behavior. Therefore, it is essential to know whether the criterion for weldability is still valid for the L-PBF printability for designing easy-to-print alloys. In this section, the printability of the most commonly studied alloys, i.e., steels, nickel-based alloys, aluminum alloys, and titanium alloys, is evaluated with special attention on the comparison with weldability. The influence of each element on the crack formation is analyzed statistically, providing fundamental knowledge for alloy design.

4.1 Fe-based alloys

The Fe-based alloys, which have been extensively studied with L-PBF, include austenitic stainless steels (304L [73, 74], 316L [43, 75, 76], etc.), precipitation hardening steels (17-4PH [77, 78], 15-5PH [79, 80], etc.), carbon tool steels (H13 [81, 82], etc.), and maraging steels (300M [83, 84], etc.).

The research emphasis of AM'ed steel was mainly on property enhancement as fully dense steel parts seem to be easily manufactured [77, 78, 85]. The mechanical properties of these steels are comparable to their conventionally made counterparts. The printability of steels is fairly satisfactory. However, the fact is that only a handful of commercial steels can be printed without cracks, which is marginal compared with more than 3 500 commercial steel grades [86] in practical applications. Furthermore, behind the decent manufacturability, numerous parametric studies have been conducted to screen out the processing window in which successful deposition is obtained. It is of great value to examine the printability of the steel alloys, aiming at exploring the key elements leading to cracks during L-PBF.

In the welding industry, the term carbon equivalent (CE) was widely accepted as an indicator to quantify the weldability of steels, as shown in **equation 1**.

$$CE = C + \frac{Mn}{6} + \frac{Cu+Ni}{6} + \frac{Cr+Mo+V}{5} (wt.\%) \qquad \text{Equation 1}$$

According to the welding industry, steels with carbon equivalent above 0.35 wt.% have poor weldability [87]. Based on the steel composition, the carbon equivalent of each steel was calculated and displayed along with their printability in **Table 1**. Surprisingly, the high carbon equivalent value does not imply poor printability as expected. On the contrary, steels with unsatisfied printability, such as tool steels, have low carbon equivalent but high carbon contents. The low carbon equivalent in tool steels calculated with Eq.1 is attributed to low Cr and Ni contents. This result demonstrates that the L-PBF printability is not merely linked to carbon equivalent, but also affected by the microstructure which is associated with all the elements in steels.

In addition to carbon equivalent, a Schaeffler diagram was widely used to estimate the phases of weld deposits based on the weldment composition, as shown in **Figure 5**. The Cr and Ni equivalents are introduced in the diagram, giving the proportions of austenite, martensite, and ferrite in the microstructure. As displayed in **Figure 5**, it is evident that the cracked steels during L-PBF mainly have martensitic microstructure, which is consistent with that observed in the weldment. Ferrite is found to resist hot cracking due to its high solubility of P and S [74]. Austenite has low solubility of P and S, thus facilitating the inter-dendritic segregation and leading to cracks [88]. Nevertheless, compared to ferrite, austenite has better ductility and a lower thermal expansion coefficient, which can reduce the risk of distortion and cracking during welding. Therefore, it is suggested to obtain ferrite-austenite bimodal phases at the end of solidification [74]. Compared with the planar grain boundaries in a single phase, the torturous inter-dendritic regions in ferrite-austenite solidification mode are more difficult for the liquid film to wet, suppressing crack propagation [74]. Compared with ferrite and austenite, martensite has limited weldability due to the high carbon content and the BCC crystal structure, which can lead to hard and brittle martensitic transformation during welding [89]. Preheating and post-weld heat treatment are generally applied to reduce the cooling rate and facilitate the formation of soft phases such as austenite, improving the ductility and toughness. As shown in **Figure 5**, the steels consisting of martensite are also more vulnerable to cracks compared to those with austenite and/or ferrite. This certifies that the effect of steel phases on weldability is consistent with that on the printability in L-PBF.

Table 1. The printability of Fe-based alloys during additive manufacturing.

Steel types	Steel name	Composition/(wt.%)									CE	Printability	Reference
		Cr	Ni	C	Si	Mn	Fe	Mo	Cu	Nb			
Austenitic stainless steel	304L	18.853	10.06	0.017	0.720	1.3	Bal	0.012	0	0	5.68	P	[74]
	316L	16.97	12.28	0.003	0.46	1.24	Bal	2.39	0.01	0	6.13	P	[43]
Martensite precipitation hardening steel	17-4PH	17.7	4.2	0.07	0.07	1	Bal	0	3.3	0.14	5.03	P	[77]
Martensitic stainless steel	15-5PH	14.65	5.01	0.043	0.61	0.578	Bal	0	3.83	0.368	4.54	P	[79]
	AISI431	16.34	1.85	0.15	0.53	0.48	Bal	0	0	0	3.81	NP	[90, 91]
	AISI420	13	<1	0.325	<1	<1	Bal	0	0	0	3.26	P	[85]
Maraging steel	14Ni-200	0.038	14.5	0.013	0.057	0.049	Bal	4.37	0.018	0	3.32	P	[92]
	L40	10.64	1.96	0.16	0.19	0	Bal	1.48	0.54	0	3.00	P	[81]
	Corrax	12	9.2	<0.05	0.2	0.2	Bal	1.4	0	0	4.30	P	[81]
	18Ni-300	0.2	18.5	0.02	0.01	0.08	Bal	5.2	0	0	4.20	P	[83]
Duplex stainless steel	AISI2205	22.88	5.45	0.028	0.333	1.818	Bal	3.105	0.224	0	6.47	-	[93]
Tool steel	H13	5.125	<0.3	0.385	1	0.35	Bal	1.425	<0.25	0	1.85	NP	[81]
	H11	5.125	0	0.4	1.025	0.4	Bal	1.35	0	0	1.76	NP	[81]
	M3:2	3.9	0	1.29	0	0	Bal	4.8	0	0	3.03	NP	[94]
	P20	1.95	0	0.4	0.45	0.83	Bal	0.33	0	0	0.99	-	[95]
	42CrMo4	1.05	0	0.415	<0.4	0.75	Bal	0.225	0	0	0.80	NP	[81]

To summarize, the printability of steels in L-PBF is influenced by key elements such as carbon and the phase constitutions. However, it should be noted that the carbon equivalent, which is commonly used to assess the weldability of steel alloys, is not valid in ranking the printability of the steels processed with L-PBF. The printability is also significantly affected by the steel microstructure. For instance, the presence of martensite in the as-printed microstructure can lead to higher susceptibility to cracking. This analysis suggests that conventional weldability may not always align with printability in L-PBF. The Schaeffler diagram is valuable in predicting steel printability with its chemistry. It is worth noticing that the Schaeffler diagram does not consider non-equilibrium solidification. During L-PBF, the elemental partitioning and the high thermal stress can induce unforeseen local phase transition, resulting in a more complex microstructure, deviating from that predicted in the Schaeffler diagram.

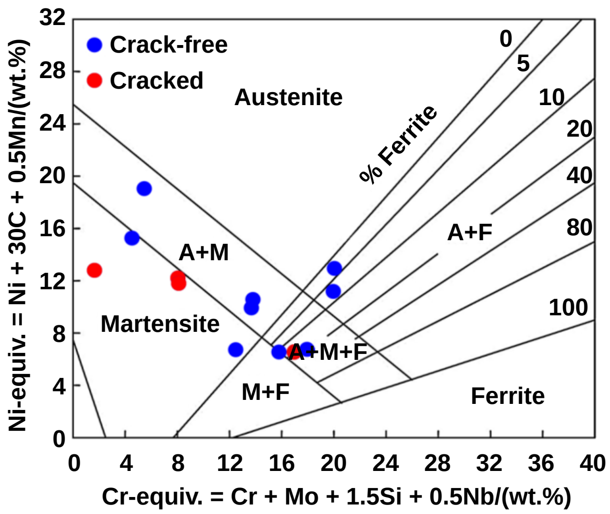

Figure 5. Schaeffler diagram with steel printability[96].

4.2 Ni-based alloys

Nickel-based superalloys generally have high strength, excellent creep resistance, and fatigue life at high temperatures [97]. They are widely used in severe high-temperature environments such as the marine and aerospace industries [98]. Conventional manufacturing of Nickel superalloys includes casting, directional casting, forging, and rolling. However, the more and more complex part structure challenges conventional manufacturing methods. A more geometry-adapted fabrication method is an urgent need. In recent years, L-PBF of nickel-based superalloy has been extensively studied and great progress has been achieved. For instance, more than 30 000 fuel nozzle tips have been successfully printed with Ni-based alloy by GE Aviation and used for LEAP engines[99]. However, the AM of nickel-based superalloys is still facing severe cracking problems. To date, only a limited amount of Nickel superalloys can be additively manufactured within a large crack-free window (the crack-free processing window is defined as the laser scanning parameter gap in which alloys can be printed without cracks and the scanning parameter can be input energy density), such as Inconel 718 and Inconel 625.

Ni-based superalloys can be strengthened by solid solution (Hastelloy X), γ’ precipitates (CM247LC et al.), and γ’’ precipitates (Inconel 718 et al.). The alloys containing high fractions of γ’ phase are known for their non-weldable behavior due to the high Al + Ti contents (>6.5 wt.%). Based on the welding industry, the nickel-based alloys containing Al + Ti > 4.5 wt.% are typically considered as non-weldable alloys [100], as shown in **Figure 6**. Haafkens *et al*. proposed a more generalized weldability assessment chart involving Cr and Co content, as shown in **Figure 7** [101]. The composition and printability of some nickel-based high-temperature alloys are shown in **Table 2**.

Considering that L-PBF is essentially similar to the welding process, it is interesting to know whether the weldability criterion is still valid for assessing printability. As shown in **Figure 6** and **Figure 7**, the cracked nickel alloys are scattered in both charts, particularly in **Figure 7** involving Cr and Co, manifesting that the printability of nickel-based superalloys is not always consistent with their weldability. For instance, the Hastelloy X (HX) and Haynes 230 were readily weldable, according to **Figure 7**. However, both alloys encounter severe cracking during L-PBF. Through efforts over the years, the crack-free Hastelloy X by L-PBF is eventually achievable (this is also the reason that HX is labeled as a printable alloy in **Figure 6** and **Figure 7**), but with strict control of minor elements. Tomus *et al.*[102] found that the HX powders with low Mn and Si contents could significantly reduce cracks during L-PBF. Later, they found that the Si and C contents played a major role in cracking mitigation as the two elements facilitated the formation of σ phase and carbides (MC, M_6C) due to the inter-dendritic segregation. Though the cracking mechanism of HX during L-PBF is still debatable, crack-free Hastelloy X powders are commercially available nowadays. Unlike HX, the cracking of Haynes 230 during L-PBF has not been completely solved without composition modification [103]. ABD900 and ABD850 are two newly developed nickel-based superalloys specifically for L-PBF [72]. Instead of having poor printability, as depicted in **Figure 7**, the two novel alloys are fairly processable during L-PBF without cracks. In the design of these two alloys, researchers considered the solidification temperature range, low melting point eutectic phases, and solid-state cracking.

The discrepancy between the printability and weldability of nickel-based superalloys is attributed to the unique processing characteristics associated with L-PBF, e.g., fast cooling rates, steep temperature gradients, cyclic heat treatment, and high thermal stresses. In conventional welding, higher Al + Ti content leads to an increased amount of γ' phase, while excessive Ti + Al can result in the precipitation of the σ phase. The σ phase acts as nuclei for the formation of harmful topologically close-packed (TCP) phases, which can lead to welding cracks. However, in L-PBF, the rapid cooling rate significantly suppresses the precipitation, resulting in lower fractions of precipitates compared to what is expected based on the Ti + Al criterion. Therefore, the traditional weldability assessment criteria, i.e., Ti + Al content, may not directly apply to printability prediction of nickel-based superalloys in L-PBF.

In summary, the conventional metal manufacturing process considers the bulk composition and relatively low cooling rates, which enables substantial elemental distribution. However, during L-PBF, the extremely fast cooling rates combined with the intrinsic heat treatment lead to a complicated near-atomic-scale composition variation, deviating significantly from the bulk composition [18]. Therefore, the bulk criterion for Ni-based alloy's weldability, e.g., (Ti + Al) %, is not always valid for the atomic-scale occasions during L-PBF. An in-depth understanding of the solute behavior at the atomic scale allows us to derive strategies to avoid cracking during laser powder bed fusion.

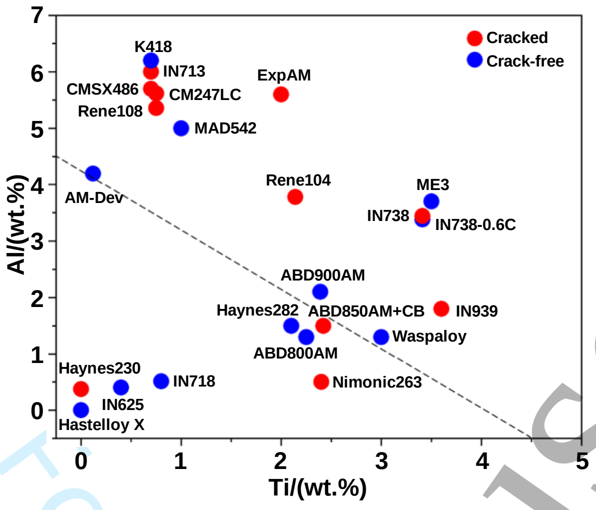

Figure 6. Correlation between printability and alloying elements in nickel-based superalloys.

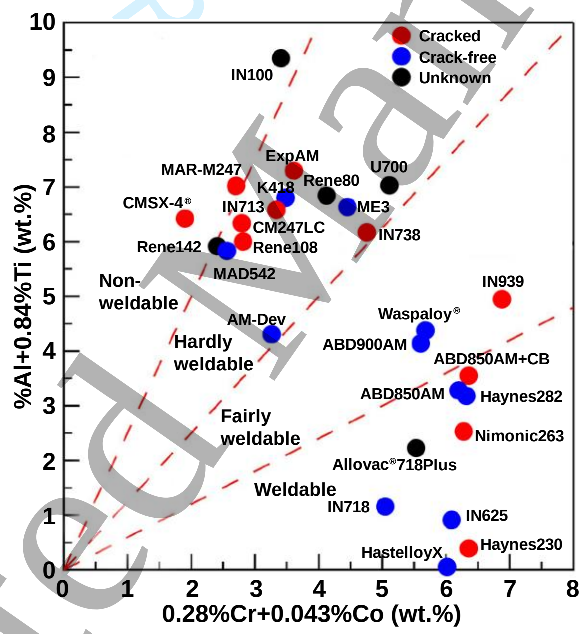

Figure 7. Effect of compositions on weldability of nickel-based superalloys. Modified weldability assessment chart after considering the effects of Cr and Co [104].

Table 2. The composition, printability and weldability of Ni-based superalloys.

Alloy	Composition/(w%)											Printability	Weldability	Reference
	Cr	Mo	Ti	Nb	Ta	W	Co	Al	C	Fe	Ni			
Inconel 718	18.5	2.91	0.8	5.11	0	0	0.01	0.51	0	17.76	54	P	W	[105]
Inconel 625	21.5	9.0	0.4	3.65	0.05	0	1	0.4	0.1	5	58	P	W	[106]
Inconel 738-0.6C	15.96	1.75	3.42	0.93	1.76	2.57	8.51	3.4	0.6	0	Bal.	P	W	[107]
Haynes 282	19.3	8.0	2.1	0	0	0	19.3	1.5	0.06	0	Bal	P	W	[108]
Haynes 230	22.81	2.1	0	0	0	14.38	0	0.37	0.11	1.86	Bal	NP	W	[109]
CM247LC	8.3	0.52	0.75	0	3.16	9.45	8.99	5.62	0.07	0	Bal	NP	NW	[72]

Inconel 738	16.04	1.75	3.41	0.99	1.75	2.49	8.59	3.44	0.133	0.13	Bal	NP	NW	[110]
Inconel 939	22.3	0	3.6	1	1.4	2	18.8	1.8	0.15	0	Bal	NP	NW	[111]
Hastelloy X	21.2	8.8	0	0	0	0	2	0	0.06	17.6	50.04	P	W	[112]
Nimonic263	19.5	2.91	2.4	0	0	0	19.2	0.5	0	0.5	Bal	NP	W	[49]
Rene 108	8.64	0.53	0.75	0	3.02	10.03	10	5.36	0.01	0	Bal	NP	-	[113]
Rene 104	12.6	3.24	2.14	2.05	0.82	3.66	20	3.78	0.05	0	Bal	NP	-	[114]
CMSX486	5	0.7	0.7	0	4.5	8.6	9.3	5.7	0.07	0	Bal	NP	NW	[115]
ABD800AM	19.9	2.02	2.25	0.64	0.48	4.85	18	1.3	0.01	0	Bal	P	-	[72]
ABD900AM	17.1	2.09	2.39	1.85	1.21	3.06	20.3	2.1	0.047	0	Bal	P	-	[72]
ABD850AM+CB	19.7	2.03	2.42	0.37	0.57	5.05	18.6	1.5	0.133	0	Bal	NP	-	[116]
ExpAM	11.7	2	2	1.1	0	3.7	7.6	5.6	0.004	0	Bal	NP	-	[116]
Waspaloy	20	0.04	3	0	0	0	12	1.3	0.05	0.04	Bal	P	-	[116]
AM-Dev	8.7	1.2	0.12	3.6	5.5	7.1	19.1	4.2	0.03	0	Bal	P	-	[116]
Inconel 713	12	4.3	0.7	2.1	0	0	0	6	0.06	0.2	Bal	NP	NW	[116]
K418	12.5	4.3	0.7	2.1	0	0	0	6.2	0.12	1	Bal	P	W	[117]
MAD542	8	5	1	2	3	4	8	5	0.1	0	Bal	P	-	[63]
ME3	13.1	3.9	3.5	1.4	2.5	1.7	18.6	3.7	0.1	0	Bal	P	-	[63]

4.3 Al-based alloys

Aluminum alloys are known for their excellent strength-density compromise and are widely used in aerospace and automobile industries, in which both lightweight and mechanical properties are needed[15]. Laser powder bed fusion of aluminum alloys enables the design of geometrically complex parts with refined microstructure and enhanced mechanical performance [118]. Most Al-based alloys currently investigated in AM are directly adopted from those developed for the conventional cast and post thermo-mechanical processes but are not optimized for AM processing. Therefore, the intrinsic rapid solidification characteristics during beam-based AM processes raise significant challenges for the manufacturing of Al-based alloys, such as the high reflectivity, hot cracking, excessive loss of volatile alloying elements due to evaporation, porosity formation, and inadequate mechanical performance for structural applications that require high strength [5, 30, 34].

High reflectivity of Al and its alloys at a laser wavelength (around 1 064 nm) necessitates a high laser energy density during L-PBF and L-DED processing to achieve a dense part [119]. The high energy input during beam-based AM processing leads to the evaporation of versatile elements. Significant vaporization losses of alloying elements, such as Zn, Mg, Li, and Mn, have been widely reported in Al-Mn (3xxx), Al-Mg (5xxx), Al-Zn-Mg (7xxx), and Al-Li-based (8xxx) alloys during laser-based AM processing due to their low boiling points (907 °C for Zn, 1 090 °C for Mg, 1 342 °C for Li, and 2 061 °C for Mn) and high equilibrium vapor pressure (Zn > Mg > Li > Mn > Al > Fe > Ni > Ti) [120, 121]. In addition, Al-based alloys suffer from porosity issues during AM processing. The formation of excessive pores is mainly related to impropriate process conditions (lack-of-fusion or keyhole pores), gas pores (vaporization of alloying elements, entrapment of shielding gases or air), and hydrogen pores (moisture, grease, or hydrocarbon contaminants) due to the significant solubility difference of hydrogen in liquid and solid aluminum [122]. Hence, optimizing the process parameter and enhancing the protective environment help in minimizing the porosity defects.

Similar to that in welding, hot cracking is one of the most critical problems in AM processing of Al-based alloys. Majority of Al-based alloys required for structural applications in aerospace and automotive industries are prone to hot cracking during beam-based AM processing. The non-weldable 2xxx series Al-Cu-Mg-based and 7xxx series Al-Zn-Mg-based, particularly Al2024 and Al7075, are not printable during AM due to their high hot cracking susceptibility [120, 123]. During conventional welding, the 5xxx series Al-Mg-based and 6xxx series Al-Mg-Si-based alloys are susceptible to hot cracking or stress corrosion cracking depending on the Mg content [124]. Fortunately, the cracking can be readily prevented by using filler metals, such as Al-Mg-Mn (Cr, Ti) (Al5356), AlMg4.5Mn0.7 (Al5183), or Al4043 (AlSi5) [65]. However, the 5xxx and 6xxx series aluminum alloys suffer from hot cracking during AM processing where filler metals are not available [125-127]. It should be noted that manufacturing crack-free 2xxx series and 6xxx series aluminum alloys using L-PBF has proven to be possible by tuning the process conditions. For instance, hot cracking of Al-Cu-Mg-Mn can be avoided during L-PBF processing using a combination of low laser power (200 W) and low scan speed (83.3 $mm \cdot s^{-1}$) due to the enhanced liquid backfilling [128]. Crack-free AA6061 parts can be manufactured using high temperature baseplate preheating at 500 °C during L-PBF due to significantly reduced thermal stresses [129, 130]. However, these strategies are not feasible solutions for widely industrial applications because the former sacrifices the production rate and the latter can cause substantial powder sintering and part oxidation. The current printable commercial Al-based alloys are limited to the 4xxx series, Al-Si-based alloys with a near eutectic composition, or 3xxx series Al-Mn-based alloys, for instance, AlSi7Mg, AlSi10Mg, and AlMn3 alloys [129, 130]. However, the low-to-medium mechanical properties of Al-Si-based and Al-Mn-based alloys could not meet the property requirements for structural applications in the aerospace and automotive industries. Therefore, there is a strong need to develop new high strength Al-based alloys tailored specifically to AM.

To design new Al-based alloys that can be processed crack-free using fusion-based AM technologies, it is crucial to identify the key influencing factors and their coupling effect on the cracking susceptibility. **Table 3** lists the chemical composition and printability during fusion-based AM processing of commonly used aluminum alloys. A Pearson correlation map was constructed to screen out the key factors responsible for the cracking of aluminum alloys, as shown in **Figure 8**. The Pearson correlation coefficient is a statistical measure used to assess the strength and direction of the linear relationship between two variables. It is calculated using the following formula:

$$\rho(x1, x2) = \frac{COV(x1,x2)}{\sigma_{x1}\sigma x2} \quad \text{Equation 2}$$

Here, ρ represents the Pearson coefficient, x1 and x2 are the two variables of interest, COV denotes the covariance between x1 and x2, and σ(x1) and σ(x2) represent the standard deviations of x1 and x2, respectively. The Pearson coefficient ranges from -1 to 1, where 1 represents a perfect positive correlation, -1 indicates a perfect negative correlation, and 0 signifies no linear correlation. By calculating the Pearson correlation coefficient, one can gain insights into the interrelationship between variables and assess the strength and direction of their association.

In this study, the Pearson correlation diagram was generated using the SciPy module in Python, incorporating data from **Table 3**. **Table 3** presents the calculated values for three features: solidus temperature (*ST*), brittleness temperature range (ΔT), and maximum solidification cracking index (SCI) at the brittleness temperature range. The SCI was calculated based on Kou's criterion [131], which was determined by the maximum slope of the T - $(f_s)^{1/2}$ curve, where f_s is the solid fraction. Brittleness temperature range (ΔT) represents the temperature range when the solid fraction is between 0.8 and 0.99 [132]. The three features were calculated using Scheil model in Thermo-Calc program with the TCAL6 and MOBAL5 database. The default phase composition, a step size of 5 °C, an ambient temperature of 25 °C, and a pressure of 10^6 Pa were used during the calculation. Once the Scheil solidification data was obtained, a Python program was written to process the exported data and calculate the three features. By examining the correlation between each element and these features, it is possible to identify the element's influence on the solidification process and its association with hot cracking. Note that this batch of alloys was not treated with the addition of secondary particles to eliminate hot cracking, as their crack elimination mechanism mainly involves grain refinement, which has little impact on the Scheil solidification curve. Therefore, they will be discussed separately in Section 5.2.3.

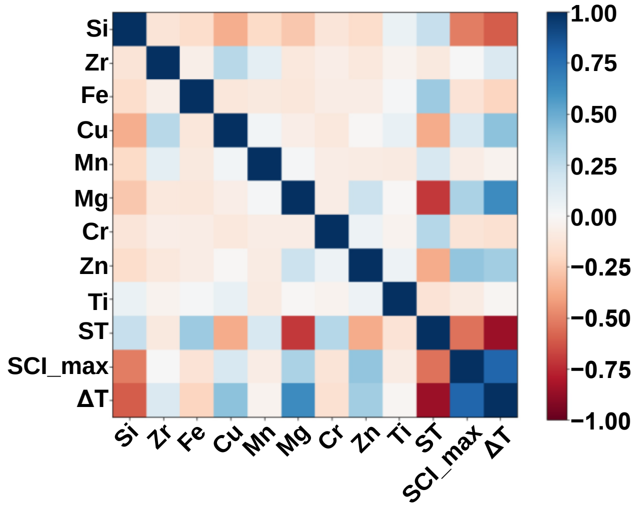

Figure 8. Pearson correlation between alloying elements and three features for aluminum alloys. *ST* represents solidus temperature, ΔT denotes brittleness temperature range when the solid fraction is between 0.8 and 0.99, and SCI max indicates the maximum value of SCI in ΔT.

As depicted in **Figure 8**, Si and Mg are the two elements that have strong correlations with the three features. Si positively correlates with solidification temperature and negatively correlates with the maximum SCI (SCI max) and brittleness temperature range (ΔT). It means that increasing Si content leads to a higher solidus and a lower SCI and ΔT, thus reducing cracks. In contrast to Si, increasing Mg content results in a decreased solidus and increased SCI and ΔT. This result implies that Mg should be lowered to reduce cracks during L-PBF. Furthermore, based on the Pearson correlation, Mg has the strongest linear correlation with ST, followed by Zn and Cu.

The specific correlations between key alloying elements on the three features were plotted in **Figure 9**. Increasing Si content raises the solidus temperature but reduces the SCI and ΔT. Higher Mg content results in a lower solidus temperature, and higher ΔT and SCI, increasing crack vulnerability, which is consistent with the Pearson correlation. Based on the statistical analysis, increasing Si and decreasing Mg are beneficial for crack mitigation for L-PBF-processed aluminum alloys. This is also in line with the experimental observations. Hyer *et al*.[133] investigated the effect of Si concentration on the cracking of Al-Si binary alloys processed via L-PBF. The results demonstrated that higher concentrations of Si in the binary Al-Si alloys exhibited lower cracking susceptibility. Moreover, Si is present as fine Si particles at low Si concentration and a web-like network of Al-Si eutectic at high Si concentration. An increase in Si concentration results in a eutectic network structure, which can act as a barrier to dislocation motion, enhancing the alloy strength. Li *et al*. [134] studied the Al-xMg-0.2Sc-0.1Zr (x = 1.5, 3.0, 6.0 wt%) alloys and found that the crack density during L-PBF increased with the Mg content. However, when 1.3 wt. % Si was added, the hot cracking disappeared due to the significantly refined microstructure and the formation of interdendritic Al-Mg_2Si.

To summarize, the aluminum alloys typically exhibited poor printability and weldability. This is primarily attributed to the large solidification temperature range, which increases the hot crack sensitivity. Furthermore, the coefficient of linear expansion in aluminum is higher compared to the other three alloy systems [135], which could induce large thermal stress and increase crack vulnerability. Pearson correlation map helps screen out the decisive factors for cracking during L-PBF of aluminum alloy among a large number of elements. Big data and statistical analysis provide a potential methodology to discover the hidden correlation between alloy chemistry and cracking susceptibility.

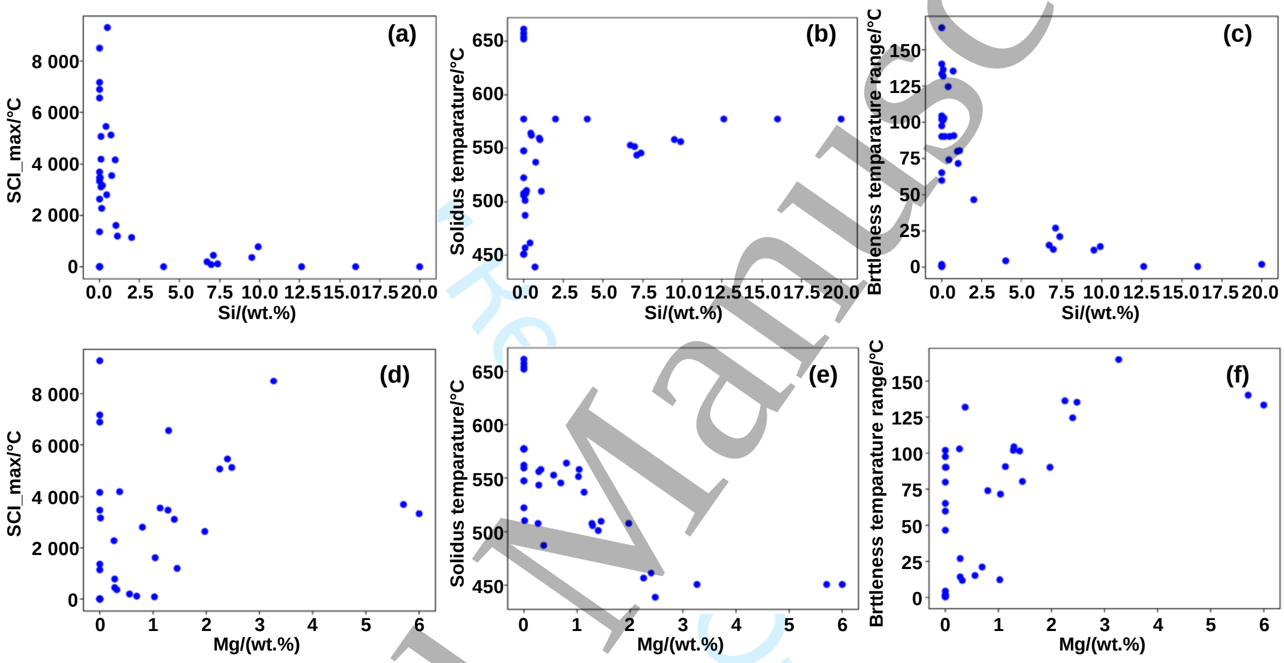

Figure 9. Effect of **(a)-(c)** Si and **(d)-(f)** Mg contents on SCI **(a, d),** solidification temperature **(b, e),** and brittleness temperature range (ΔT) **(c, f)** of aluminum alloys.

Table 3. The solidus temperature, maximum SCI, brittleness temperature range, and printability of commonly seen aluminum alloys.

Alloy	Composition(wt.%)											**Solidus temperature /°C**	**Maximum SCI/°C**	**Brittleness temperature range/ °C**	**Printability**	Reference
	Al	Si	Zr	Fe	Cu	Mn	Mg	Cr	Zn	Ti	Ni	Li					
AlCu2	Bal	0	0	0	2	0	0	0	0	0	0	0	547.5	6 895.8	97.6	NP	[136, 137]
AA2022	Bal	0.15	0	0.2	5	0.325	0.275	0.05	0.175	0.15	0	0	507.5	2 263.7	103.3	NP	[138]
AA2024	Bal	0.06	0	0.13	3.9	0.41	1.29	0	0	0	0	0	507.4	3 472.1	102.0	NP	[123]
AA2139	Bal	0.10	0	0.20	4.20	0.40	1.40	0	0.20	0	0	0	500.9	3 092.0	101.5	NP	[139]
AA2195	B	0.	0.	0	4.	0	0.	0	0	0	0	1.	487.1	4 188.7	132.0	NP	[140]

	al	12	13		00		38					00					
AA2219	Bal	0.2	0.175	0.3	6.3	0.3	0.02	0	0.1	0.051	0	0	510.3	3 169.0	90.2	P	[141]
AlCu6.8	Bal	0	0	0	6.8	0	0	0	0	0	0	0	547.6	1 368.2	59.6	P	[136, 137]
AlCuMgMn	Bal	0	0	0	4.24	0.56	1.97	0	0	0	0	0	507.7	2 633.2	90.2	P	[128]
AlCuMgNi	Bal	0	0	1.2	2.5	0	1.3	0	0	0.07	1.2	0	506.0	6 564.9	104.3	P	[142]
Al-Cu-Mg-Si	Bal	1.12	0	0	3.56	0.62	1.45	0	0	0	0	0	509.7	1 206.5	80.5	P	[143]
Al-Cu-Li	Bal	0	0	0	4.0	0	0	0	0	0	0	1.25	522.1	3 467.8	102.2	NP	[144]
AlMn3	Bal	0	0	0	0	3	0	0	0	0	0	0	657.2	2.4	0.2	P	[129]
AlCr3	Bal	0	0	0	0	0	0	3	0	0	0	0	661.0	0.7	1.4	P	[129]
AlFe3	Bal	0	0	3	0	0	0	0	0	0	0	0	654.2	2.4	0.2	P	[129]
AlFe2.5	Bal	0.03	0	2.55	0	0	0	0	0	0	0	0	652.0	0.5	2.1	P	[145]
A356 (AlSi7Mg0.3)	Bal	7.12	0.03	0.16	0.01	0.005	0.29	0	0.03	0.005	0	0	543.5	454.9	27.0	P	[146]
A357	Bal	7.37	0	0.15	0.005	0	0.7	0	0.005	0.005	0	0	545.5	111.5	21.2	P	[147]
F357	Bal	7	0	0.15	0.05	0.03	1.025	0	0.05	0.2	0	0	551.4	101.5	12.3	P	[148]
AlSi7Mg0.6	Bal	6.7	0	0.08	0.025	0.005	0.57	0	0.005	0.1	0	0	552.5	209.5	14.9	P	[149]
AlSi10Mg（CL31)	Bal	9.5	0	0.275	0	0.225	0.325	0	0	0.075	0	0	557.8	357.0	11.7	P	[69]
AlSi10Mg	Bal	9.92	0	0.137	0	0.004	0.291	0	0.01	0.006	0.04	0	556.1	787.4	14.3	P	[150]
AlSi0.5	Bal	0.5	0	0	0	0	0	0	0	0	0	0	562.2	9 278.5	90.2	NP	[133]
AlSi1	Bal	1	0	0	0	0	0	0	0	0	0	0	559.2	4 155.8	80.2	NP	[133]
AlSi2	Bal	2	0	0	0	0	0	0	0	0	0	0	576.9	1 131.7	46.4	NP	[133]
AlSi4	Bal	4	0	0	0	0	0	0	0	0	0	0	576.9	1.1	4.1	P	[133]
AlSi12.6	Bal	12.6	0	0	0	0	0	0	0	0	0	0	576.9	0.2	0.2	P	[133]
AlSi16	B	16	0	0	0	0	0	0	0	0	0	0	576.9	0.2	0.2	P	[133]

	al															
AlSi20	Bal	20	0	0	0	0	0	0	0	0	0	0	576.9	2.5	1.8	P	[151]
AA5083	Bal	0	0	0.41	0	0.88	3.27	0	0	0	0	0	450.6	8 480.5	165.3	NP	[127]
AlMg5.7	Bal	0	0	0	0	0	5.7	0	0	0	0	0	450.6	3 691.7	140.2	P	[136, 152]
AlMg6	Bal	0	0	0	0	0	6	0	0	0	0	0	450.6	3 333.1	133.7	P	[136, 152]
AA6061	Bal	0.78	0	0.28	0.21	0.09	1.14	0.24	0.06	0.11	0.1	0	536.9	3 534.3	90.8	NP	[153]
AA6063	Bal	0.45	0	0.25	0	0	0.8	0	0	0	0	0	563.9	2 802.4	73.9	NP	[154]
AA6182	Bal	1.02	0.18	0.11	0	0.79	1.04	0	0	0	0	0	557.7	1 616.3	71.5	NP	[155]
AA7050	Bal	0.4	0	0.11	1.56	0.26	2.4	0.25	5.54	0	0	0	461.3	5 446.8	124.6	NP	[120]
AA7075	Bal	0.13	0	0.17	1.54	0.02	2.25	0.19	5.4	0.005	0	0	456.7	5 060.8	136.3	NP	[69]
AA7075	Bal	0.727	0	0.19	1.64	0.053	2.48	0.263	6.52	0.095	0	0	438.6	5 129.8	135.4	NP	[156]
AlZn5	Bal	0	0	0	0	0	0	0	5	0	0	0	577.0	7 150.7	65.0	P	[136, 137]

4.4 Ti-based alloys

Titanium alloys, possessing desired strength, biocompatibility, and excellent corrosion resistance, have been widely used in biomedical, aerospace, and defense industries. Depending on alloying elements, titanium alloys can be classified as α, near α, α – β, near β, β-titanium, and metastable β titanium alloys [71]. Conventional titanium producing processes include forging, casting, and powder metallurgy. Machining is generally needed to achieve the final geometry of the parts. However, titanium alloys are known as hard-to-machine materials due to their low Young's modulus and thermal conductivity, hindering their wide application in diverse industries [157]. As L-PBF is a near-net shaping technology, manufacturing hard-to-machine materials such as titanium alloys has drawn extensive attentions.

The easy-to-print titanium alloys include CP-Ti, which is pure titanium, and Ti6Al4V. The additive manufacturing of CP-Ti initially faces the impurity problem, particularly in controlling the oxygen level as titanium can form strong bonding with oxygen. Recent studies demonstrated that the oxygen content can be well-controlled, and the density of CP-Ti can achieve 99% [158]. Another titanium alloy that has been extensively studied in the AM community is Ti6Al4V, which is a typical α–β alloy. The as-fabricated

Ti6Al4V has predominantly refined α' martensite through the β to α' martensitic transition, leading to a higher yield strength (>1 100MPa), but a lower elongation to failure (5% ~ 10%), compared to the wrought alloy [71]. Lu *et al*. [159] found that the tensile strength is determined by the content of fine α' martensite and lath thickness, while plasticity is influenced by prior β grain size and lath length. Increasing α' fraction and refining prior β grains and α laths simultaneously improves strength and plasticity. Wang *et al*. [160] improved the ductility and mechanical isotropy by reducing the Al content in Ti6Al4V from 6 wt.% to 4 wt.%. This is due to the activation of multiple slip modes and twins during solidification and deformation. Chen *et al*. [161] utilized blended powders of Ti6Al4V and 3 wt.% Fe particles during L-PBF. The as-built microstructures transit from α' dominated microstructure to a nearly complete β-dominated microstructure, exhibiting high strength and enhanced ductility without post-heat treatments. Seunghee A *et al*. [162] obtained martensitic α' and α + α' + β microstructures by utilizing two different laser scanning speeds. The critical cooling rate of fully martensitic transformation is in the range between 2 900 and 6 500 $°C·s^{-1}$. Although Ti6Al4V is widely used due to its inherent resistance to in-vivo corrosion, favorable osteointegration properties, and excellent strength-to-weight ratio, the release of toxic vanadium (V) ions in the human body poses health risks [163]. Issariyapat *et al*. [164] investigated the Ti-Zr alloy as a substitute for Ti6Al4V. They successfully prepared high-density Ti–Zr materials with homogeneous Zr distribution through laser powder bed fusion (L-PBF) using pre-mixed blends of Ti 0 ~ 10 wt% ZrH_2 powders. The presence of Zr promoted grain refinement, resulting in a fine acicular grain structure. Increasing Zr content significantly enhanced the tensile yield strength, while maintaining acceptable ductility. Ti-6Al-7Nb alloy, which replaces V with Nb in its composition, exhibits a martensitic α' phase hardened by dispersed precipitates. Chlebus *et al*. [165] studied the effect of L-PBF manufacturing strategy on the mechanical properties and microstructure of Ti-6Al-7Nb alloy and found higher tensile and compressive strength but lower ductility compared to conventional methods. Ti-24Nb-4Zr-8Sn (Ti2448) is a near β-Ti alloy with a low Young's modulus (42 ~ 50 GPa) [166]. Introducing porosity further reduces the Young's modulus [167], making it suitable for porous titanium structures that match the human skeleton (4 ~ 30 GPa), which can be produced using L-PBF [168].

As discussed above, different from nickel-based and aluminum alloys, studies on the crack formation and mitigation of titanium alloys during L-PBF are rarely reported in literature, suggesting a good printability of titanium alloys. Compared to nickel-based superalloys, titanium alloys have lower Young's modulus [169]. The low Young's modulus enables titanium alloys to accommodate larger strains during L-

PBF. Such large deformation of titanium releases the high residual stress accumulated during intrinsic heat treatment of L-PBF process, alleviating the stress concentration and thus cracking behavior. Therefore, fully dense titanium alloys are achievable by optimizing scanning parameters, as shown in **Table 4**. The laser powder bed fusion of titanium alloys mainly focuses on suppressing epitaxial grain growth of long columnar grains, enhancing mechanical properties, and designing lattice structures for energy absorption and biomedical applications. A molybdenum equivalent MoE is also widely used to analyze the phase constitutions of titanium alloys, as shown in **equation 3**. If $0 \leq \text{MoE} < 5$, the titanium alloy is rich in β phase. If $5 \leq \text{MoE} < 10$, the alloy is near β phase. The alloy is metastable in the case of $10 \leq \text{MoE} < 30$, whereas for $\text{MoE} > 30$, alloys are considered stabilized.

$$MoE = 1.0(wt.\%\,Mo) + 0.67(wt.\%\,V) + 0.44(wt.\%\,W) + 0.28(wt.\%\,Nb) + 0.22(wt.\%\,Ta) + 2.9(wt.\%\,Fe) + 0.28(wt.\%\,Nb) + 0.22(wt.\%\,Ta) + 2.9(wt.\%\,Fe) + 0.28(wt.\%\,Nb) + 0.22(wt.\%\,Ta) + 2.9(wt.\%\,Fe) \quad \text{Equation 3}$$

Table 4. The composition, types, MOE and printability of Ti-based alloys.

Alloy	composition(w%)												Classification	Molybdenum equivalent MoE	Printability	Reference
	Ti	Al	V	Nb	Mo	Cr	Fe	Zr	C	Si	Ta	Sn				
Ti6Al4V	Bal	5.77	4.15	0.04	0.07	0	0.34	0	0	0.02	0	0.08	α+β	9.62	P	[170]
Ti6Al7Nb	Bal	5.5	0	6.8	0	0	0.25	0	0	0	0	0	α+β	8.13	P	[165]
Ti2448	Bal	0	0	24	0	0	0	4	0	0	0	8	Near β	6.72	P	[171]
Ti1023	Bal	3	10	0	0	0	2	0	0	0	0	0	Near β/Metastable β	15.50	-	[171]
Ti5553	Bal	5	5	0	5	3	0	0	0	0	0	0	Near β	18.15	P	[171]
Beta C	Bal	3	8	0	4	6	0	4	0	0	0	0	Metastable β	21.96	-	[171]
Alloy C	Bal	0	35	0	0	15	0	0	0	0	0	0	Stable β	47.45	-	[171]
Ti-13Nb-13Zr	Bal	0	0	12.66	0	0	0	13.12	0	0	0	0	β-rich	3.54	-	[172]
Ti-35Nb-5Ta-7Zr	Bal	0	0	34.5	0	0	0	6.5	0	0	4.5	0	β	10.65	-	[173, 174]
Ti-12Mo-6Zr-2Fe	Bal	0	0	0	12	0	2	6	0	0	0	0	β	17.80	P	[175]
Ti-5Al-5Mo-5V-1Cr-1Fe	Bal	5.2	5	0	4.93	1.1	0.96	0.01	0.01	0.02	0	0	Near β	18.02	P	[176]

Ti-6242	Bal	6	0	0	1.92	0	0.05	3.93	0.01	0	0	1.89	Near α	8.07	P	[177]
Ti-6246	Bal	6	0	0	6	0	<0.15	4	<0.04	0	0	2	Near β	12.00	-	[178]

As discussed above, titanium alloys generally have fewer cracking problems during L-PBF comparing to Ni-based and Al-based alloys. This can be attributed to the smaller number of elements, which results in fewer low-melting-point precipitates at grain boundaries. Moreover, Ti-based alloys generally have a narrower solidification temperature range and a lower Young's modulus, which further reduces the hot crack sensitivity. Similarly, the weldability of titanium alloys is also quite satisfactory comparing to the other three alloy systems investigated in this work.

To summarize, while L-PBF offers numerous advantages, such as the ability to create complex geometries and produce functional metal parts, several specific issues can arise when using existing alloys in L-PBF.

(1) **Defects**: During the L-PBF process, rapid and localized heating and cooling cycles induce significant thermal stress in the printed part. This thermal stress can cause cracking and distortion, as existing alloys are not specifically designed to resist such stress during the forming process. Alloys with narrower solidification ranges tend to exhibit better printability, while those with large solidification ranges like CM247LC and AA7075 are more prone to cracking during L-PBF. Alloys with higher thermal conductivity can dissipate heat more efficiently, reducing the risk of thermal stress build-up and cracking. Mismatched thermal conductivities can lead to thermal gradients, warpage, and residual stresses, affecting part quality. Additionally, L-PBF requires high-quality powders as feedstock. Powder characteristics, such as normally distributed particle size, spherical morphology, and excellent flowability, are required to achieve desired print quality. However, not every conventional alloy can be processed into powders that meet these requirements. Powders with entrapped gas, undesirable morphology, or poor flowability can lead to defects such as porosity and lack-of-fusion in the printed part.

(2) **Compositions**: The alloy impurity in conventional processes can be reduced to extremely low levels using specific equipment like vacuum degassing furnace. However, in the powder-making process, the lack of specialized equipment or contamination from the refractory materials used during powder-making could increase the impurity levels in the powders. Additionally, the use of certain alloying elements with low melting point in conventional alloys, such as Mg and Al, can lead to issues like excessive powder spattering or vaporization during laser exposure. Furthermore, despite flushing the L-PBF equipment with inert gases

before printing, there might still be residual oxygen atoms present. This can result in oxidation of alloys that are prone to oxidation, which can degrade their mechanical properties. It is important to note that alloys highly reactive with oxygen, moisture, or other environmental gas, such as Mg, should be printed with specialized equipment or in controlled environments.

(3) **Microstructure**: Due to layer-wise build-up manner during L-PBF, the epitaxial grain growth is facilitated, leading to columnar grains along the building direction, which is undesirable for conventionally designed equiaxed grain structures. The rapid solidification during L-PBF can result in finer microstructures, but it can also lead to some metastable phases. The intrinsic heat treatment occurring during L-PBF can further contribute to the formation of undesirable phases, necessitating additional post-processing like heat treatment.

(4) **Post-Processing**: L-PBF parts often require post-processing steps such as heat treatment, hot isostatic pressing, or surface finishing to achieve the desired properties. However, these steps may differ from the conventional post processing optimized for casted or wrought alloys. Therefore, additional research and process optimization are required to develop post-processing techniques suitable for L-PBF fabricated parts using existing alloys.

(5) **Mechanical properties**: L-PBF fabricated parts exhibit anisotropic mechanical properties due to the layer-by-layer building process. The microstructure anisotropy might limit their performance in certain applications. Furthermore, the LPBF-processed traditional alloys might have reduced ductility and lower fatigue resistance due to the formation of fine-grained or non-equilibrium microstructures.

5. Alloy design strategies for L-PBF

As discussed above, using existing alloys developed for conventional casting and forging processes in L-PBF can be challenging due to differences in solidification behavior, microstructure, properties, and post-processing requirements. To fully leverage the capabilities of L-PBF, it is crucial to develop alloys specifically designed for this technique.

Commercial alloys are designed for specific applications. The mechanical properties of commercial alloys have been certified and well-known. It is undesirable to modify the alloy composition as this would lead to deterioration of the mechanical performance. However, as discussed in section 4, the existing alloys are designed for traditional alloy-making processes without AM in mind. Consequently, server cracking is constantly observed in most of the commercial alloys processed with AM, particularly the L-PBF. Multiple works attempt to modify the commercial alloy composition within the specification to improve printability. This is conservative as it is challenging to completely remove all the cracks in this way although it does not need to undergo an additional certification process. Some newly designed alloys achieve great success in crack mitigation, such as ABD900-AM [72], a novel nickel-based superalloy tailored for the L-PBF process. However, a knowledge-based alloy design guideline specifically for L-PBF is still absent. Three primary strategies are found in the literature. With mechanical properties in mind, one focuses on crack mitigation by studying the cracking mechanism, and the second tends to refine the grain structure. The third strategy employs the recently popular machine learning process without an in-depth understanding of the cracking or grain refining mechanism.

5.1 Crack mitigation-oriented strategies

Even in conventional casting, the mechanism of cracking is still under debate, although this topic has been studied extensively for years [179]. With the advance of AM, the attention on the cracking mechanism has been raised again. A lot of efforts have been spared on designing crack-free alloys for the L-PBF process. In this section, the crack criteria used during alloy design was presented at first. Subsequently, the grain and cell boundary manipulation work were reviewed as most of the crack-mitigation work focuses on the grain/cell boundary manipulations.

5.1.1 Cracking criteria

As discussed in section 3.2, cracks in LPBF-processed metals are classified as hot cracking, i.e., solidification cracking and liquation cracking, and solid-state cracking, which includes strain-age cracking (SAC) and ductility-dip cracking (DDC).

Various theories have been proposed to explain the formation of hot cracking during L-PBF, such as the RGD theory [180], Kou's criterion [131], solidification temperature range/freezing temperature range (temperature difference between liquidus and solidus), and brittleness temperature range (solid fraction between 0.8 and 0.99) [132].

Rappaz-Drezet-Gremaud (**RDG**) criterion for cracking is widely applied in L-PBF[180]. According to this criterion, hot tearing occurs if the pressure within the semi-solid mushy zone drops beyond a critical value. Besides, a viscous liquid is more difficult to flow and backfill the existing porosity or crack at the end of solidification. In the RDG model, the grain boundary can be categorized into repulsive (stabilization of liquid films) and attractive boundaries (dendrite coalescence). The coalescence undercooling is found to be higher at high angle grain boundaries (HAGBs) than at low angle grain boundaries (LAGBs), indicating that the liquid film at HAGBs is stable at lower temperatures. This is consistent with the experimental observation that cracks are found to propagate along high angle grain boundaries, which is similar to welding [61].

Clyne and Davis [181] considered the time duration of the solidification intervals at high temperatures (between 10 ~ 60 vol.% liquid, t_r, indicating the time available for stress relaxation) and low temperatures (between 1 ~ 10 vol.% liquid, t_v, indicating the vulnerable time when cracks can propagate easily). The ratio of t_v/t_r is defined as the hot-cracking sensitivity (HCS). This model has succeeded in predicting the cracking susceptibility in aluminum alloys[180].

Xu *et al.*[63] proposed a heat resistance and deformation resistance (**HR-DR**) model for nickel-based superalloys processed via L-PBF. In this model, cracks are attributed to low heat resistance and deformation resistance at grain boundaries. Heat resistance (HR) is linked to the solidus temperature difference between the interdendritic (ID) and the dendritic core (DC) region. Deformation resistance (DR) is associated with the difference in the yield strength between DC and ID. According to the HR-DR model, alloying elements such as Zr, B, and Hf dramatically reduce the cracking resistance due to their strong segregation to inter-dendritic regions. Moreover, the γ' fraction has limited influence on the L-PBF as their precipitations are suppressed during the rapid cooling in L-PBF. The HR-DR model has been successfully validated using a novel nickel alloy MAD542 [182] and the commercial Rene 104 (also termed as ME3).

Another widely used cracking criterion was proposed by **Kou** [131], who considered the correlation amongst 1) separation of grains from each other due to solidification contraction, 2) the growth of two neighboring grains toward each other, and 3) the liquid backfilling between the intergranular channel. Based on these understandings, Kou derived an SCI to evaluate the hot cracking vulnerability of an alloy during solidification, as shown in **equation 4**.

$$SCI = \left| dT/d(f_s^{1/2}) \right| \qquad \text{Equation 4}$$

where T is the temperature and f_s is the fraction of solid. The index was successfully verified with experimental data in casting and welding of Al alloys [131]. Additionally, Tang *et al.* [72] calculated the SCI of nickel-based superalloys, and found that the SCI of CM247LC, Inconel 939 and Inconel 738LC was significantly higher than those easy-to-print alloys such as Inconel 718, which was consistent with the experimental observation.

Solidification temperature range/freezing temperature range has been widely employed to qualitatively assess the printability of alloys during L-PBF. Griffiths *et al*. [183] found that decreasing Hf significantly reduces the solidification temperature range of the nickel-based superalloy CM247LC. A Hf-free version of CM247LC was developed with crack density reduced by 36% ~ 75%. Tomus *et al*. [102] used two batches of pre-alloyed Hastelloy-X powders with different Si, Mn, and C contents for L-PBF. It was found that low Si and C contents reduced the solidification interval, helping to avoid crack formation. Therefore, by lowering Si and C content, crack-free Hastelloy X was fabricated via L-PBF. In terms of aluminum alloys, it is found that introducing silicon to aluminum alloys such as 2 024, 6 061, and 7 075 can eliminate cracks due to the reduced solidification range, thermal expansion, and solidification shrinkage [184]. However, the solidification temperature range is not always valid in interpreting cracks. For instance, Zhao *et al*. [103] found that the addition of Zr (1 wt.%) in Haynes 320 resulted in a higher solidification temperature range. Instead of increasing hot crack sensitivity, the cracking was completely suppressed. Similarly, Sun *et al*. [185] introduced Al element into a high-entropy alloy CoCrFeNi, which was crack susceptible. Although the solidification temperature range was enlarged, adding 0.5wt.% Al significantly decreased the crack density. This was attributed to the grain boundary phase formation that lowered the tensile stress or even altered the stress state at the grain boundaries.

5.1.2 Grain\cell boundary manipulation

The in-depth characterization of cracks demonstrates that grain boundaries and cell boundaries are the most vulnerable regions for cracking in L-PBF-processed microstructure. The rapid solidification during L-PBF leads to a supersaturated solid solution matrix. On top of that, the solutes that partition into the inter-dendritic liquid are insufficient to equilibrate via diffusion. This results in elemental enrichment at the solidification front based on the classical constitutional undercooling theory. The elemental enrichment assists the formation of intermetallics, carbides, or oxide inclusions, as shown in **Figure 10**. In casting, the intermetallic is beneficial for preventing hot cracking [186]. However, in the L-PBF process, the intermetallic at grain boundaries might be detrimental to the grain boundary integrities [187]. The occurrence of cracking during L-PBF is tightly associated with their boundary characteristics. Therefore, the concept of grain boundary segregation engineering was employed to manipulate the grain boundary features to counteract the cracking problems in metal additive manufacturing [185].

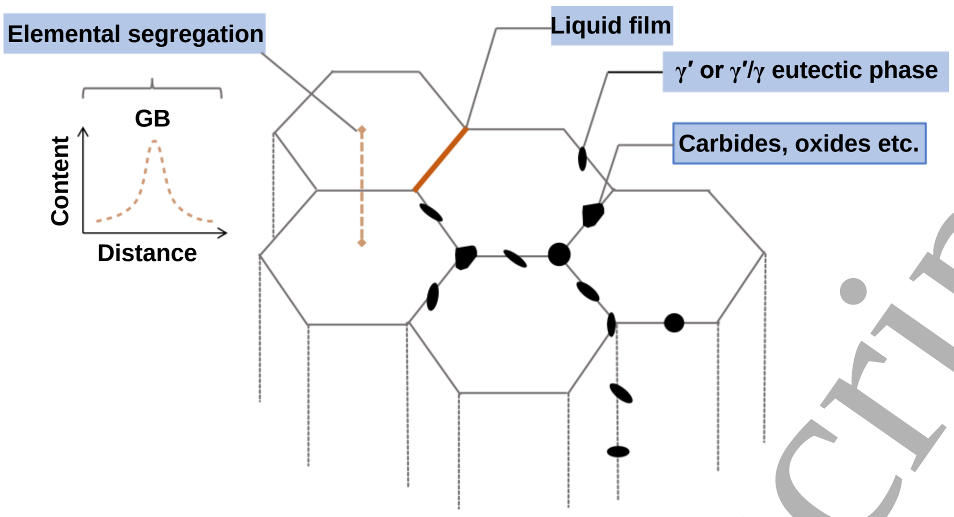

Figure 10. Grain boundary features during laser powder bed fusion additive manufacturing.

Sun *et al.*[185] found that the elemental segregation lead to a liquid film at the grain boundary at the end of solidification. Consequently, discontinuous precipitates formed along the grain boundary. The precipitates could accommodate the tensile residual stress through grain deformation and molar volume expansion. The tensile stress could thus switch into compressive stress, suppressing the formation of cracks, as displayed in **Figure 11**(d). However, when the brittle precipitates form a continuous film, they promote crack initiation instead of acting as strain absorbers. Later, they developed a thermodynamics-guided approach for L-PBF alloy design using the concept of grain boundary segregation engineering [188]. The authors solved the hot cracking problem of Inconel 738LC alloy through lowering the Si content from 0.11 wt.% to 0.03 wt.%. They concluded that the occurrence of hot cracking during L-PBF required (a) pores to act as crack nucleation sources and (b) liquid films with a low solidus temperature to facilitate crack propagation, i.e., B in their work. Zhou *et al.*[107] found that with the carbon content increase from 0.11 wt.% (Inconel 738LC) to 0.3 wt.% and 0.6 wt.%, crack-free Inconel 738 was produced in a wide range of L-PBF parameters (76 ~ 126 $J \cdot mm^{-3}$). With the increase in carbon content, the γ/γ' eutectic decreased, and the cracking sensitivity decreased correspondingly (**Figure 11**(a)).

Kontis *et al.*[18] found that a segregated film at a HAGB can switch into a liquid film, as depicted in **Figure 11**(b). The local thermal stresses and segregation-induced grain boundary liquation jointly cause hot cracking. Fewer grain boundaries lead to more concentrated and continuous liquid films extending over several millimeters, which is detrimental to mechanical performance. Therefore, they proposed to obtain an equiaxed or a columnar microstructure with a grain width smaller than 100 μm to avoid cracking, despite strong grain boundary segregation.

Thapliyal *et al*. [189] proposed a theoretical framework applying the concept of segregation engineering of grain boundaries during L-PBF. In order to use the proposed framework, the authors address the premises, which are: (a) certain elements must segregate at grain boundaries due to the low solid solubility, (b) solute segregation at the grain boundaries leads to reduced energy and mobility of the boundaries, and (c) segregation of the solute may lead to either an enhanced or deteriorated boundary cohesion depending on whether the solute is of strengthening or embrittling type (**Figure 11**(c)). They explored the concept to facilitate microstructural heterogeneity and hierarchy, suppressing cracking-susceptible columnar growth and leading to good printability at a wide range of process parameters.

Unlike most studies, in which researchers attempted to reduce the liquid film at grain boundaries, Zhao *et al*. [103] introduced liquid backfilling and a network of segregation phases at grain boundaries to alleviate thermal stress. Following this strategy, they added Zr in Haynes 230 and obtained crack-free specimens with an extraordinary combination of strength and plasticity.

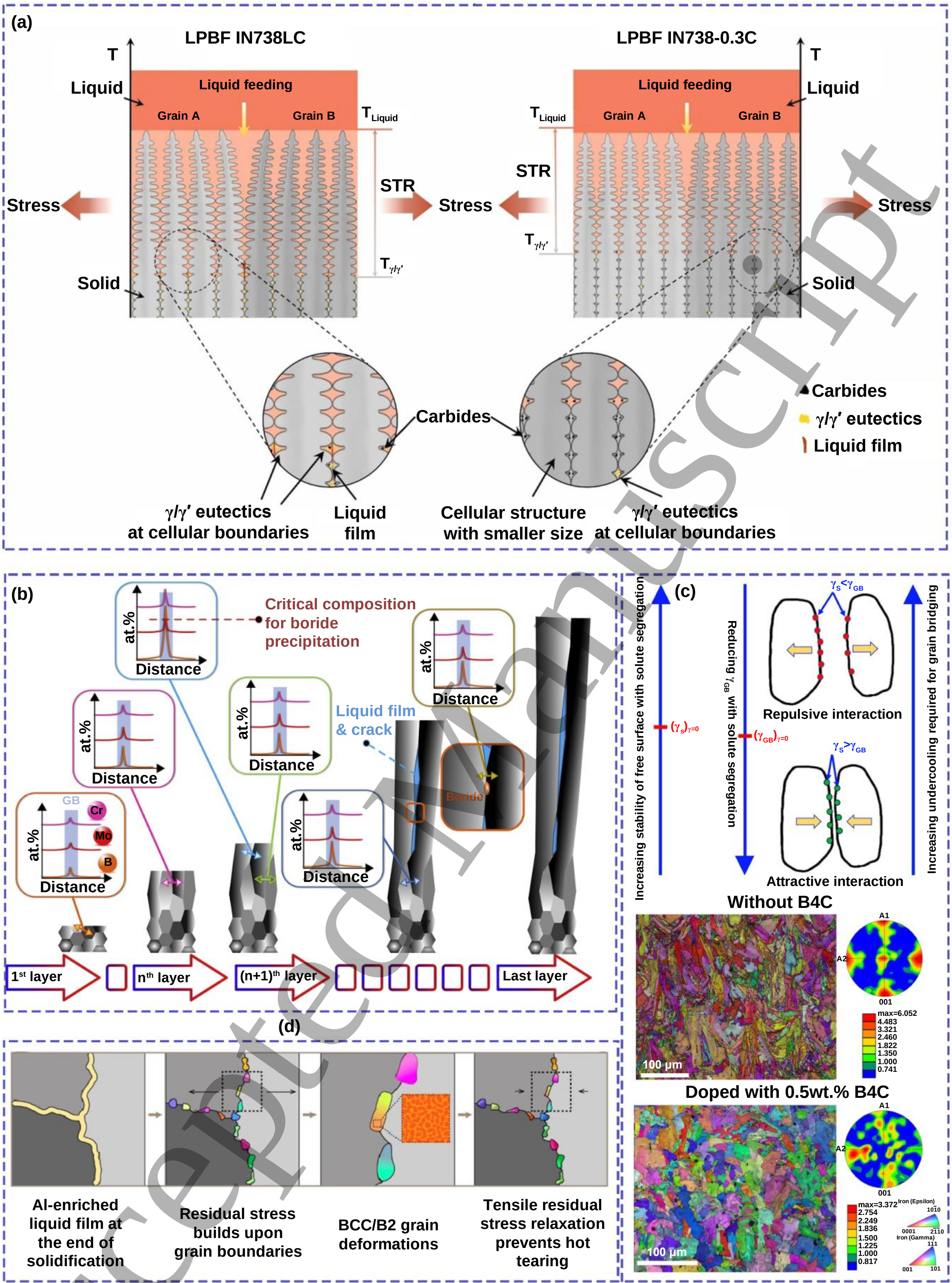

Figure 11. Suppressing cracks during L-PBF using the concept of grain boundary segregation engineering. **(a)** Schematic of the inhibition effect of carbon on the cracking of L-PBF Inconel 738. The addition of carbon reduces the enrichment of element B at grain boundaries and decreases the formation of low-melting-point phases[107]. **(b)** Schematic of the microstructural and compositional evolution during AM of the superalloys with hot cracks. The progressive enrichment in Cr, Mo and B at grain boundaries over the building process causes grain

boundary segregation induced liquation [18]. **(c)** Schematic of solute segregation effect on interfacial energy and solidification behavior of metastable Fe-Mn-Co-Cr-Si high entropy alloy processed via L-PBF [189]. **(d)** Schematics of residual stress minimization for Al0.5CoCrFeNi alloy during L-PBF. The image indicates the Al segregation towards the interdendritic/grain boundaries, discontinuous BCC/B2 grains formed along the grain boundaries, the tensile residual stress accommodated by the BCC/B2 grains, and the switch from a large tensile residual strain a small compressive residual strain[185].

To summarize, the rejection of solutes during rapid solidification in L-PBF leads to cell/dendrite segregation. The enrichment of solutes in the residual liquid reduces the grain boundary energy and mobility and affects the grain boundary cohesiveness. Depending on whether the solute is of strengthening type or embrittling type, the grain boundary is then strengthened or easily cracked. Moreover, the segregation-induced grain boundary characterization can lead to the low-melting-point phase formation, which is not desired considering the hot cracking. Nevertheless, the precipitates can also reduce the detrimental effect of residual thermal strain and facilitate liquid backfilling, which are beneficial for cracking mitigation. Therefore, the grain boundary segregation should be carefully manipulated in order to design novel crack-free alloys for L-PBF.

5.2 Microstructure manipulation-oriented strategies

In section 5.1, we summarized the work on designing alloys for L-PBF with the intention of removing cracks. However, crack mitigation is not the sole purpose of alloy design for L-PBF. In addition to cracks, the microstructure of LPBF-processed alloys also significantly impacts the mechanical properties, corrosion resistance and other functional properties, thus affecting the alloy's application. Generally, the layer-by-layer printing nature of the L-PBF process is favorable for the columnar grain growth. Columnar microstructures, ideally single crystalline, are desirable for applications such as gas turbine blades to enhance creep and fatigue properties. However, in most cases, microstructure anisotropy is undesirable, and a refined and equiaxed microstructure is preferred. Furthermore, due to the fast cooling rate, the as-built alloys are constantly a supersaturated solid solution. While this may be favorable for solid solution alloys, precipitation hardening alloys typically require post-heat treatment to achieve optimal properties. Therefore, when designing alloys for the L-PBF process, it is crucial to consider the microstructure preferences of the specific alloy. By accounting for the desired microstructural characteristics during alloy design, extensive parameter optimization work and post-heat treatment can potentially be avoided, simplifying the overall manufacturing process.

The high cooling rate and high thermal gradient of laser powder bed fusion almost exclusively lead to columnar grains, which are undesirable considering the anisotropic mechanical properties in most of the applications [190]. According to the well-established grain refinement theory in casting, nuclei provide a site for growth, and solute leads to constitutional supercooling, which activates adjacent nuclei [191]. A growth restriction factor, Q, defined as the development rate of a constitutionally undercooled zone, is employed to assess the effect of an element on grain refinement [192]. Tan *et al*. [193] reconsidered the grain refinement theory and found that the classic theory (i.e., Q value) could not be directly applied to metal L-PBF. The large thermal gradient during L-PBF could significantly inhibit the formation of a compositional supercooling zone ahead of the S/L (solid/liquid) interface. In addition, the solute rejection resulted in a lag in the actual growth of the S/L interface compared to the theoretical solidification rate. The growth restriction factor (Q value) cannot characterize the role of solutes in L-PBF. Despite the lack of exact grain refinement theories, a considerable amount of work has been reported in the literature, achieving refined microstructure in newly designed or tailored commercial alloys for L-PBF. Three different strategies were found in the literature to promote the columnar-to-equiaxed (CTE) transition during L-PBF, i.e., optimizing process parameters such as in steels [194, 195] and nickel-based alloys [196], the addition of solute elements with a high supercooling capacity like in titanium alloys [190, 197-200], and exploring grain refiners for aluminum alloys [201-206].

In this section, the microstructure manipulation-oriented strategies were discussed, including phase transition, columnar-to-equiaxed transition, and grain refinement. Phase transition involves making use of the rapid cooling and intrinsic heat treatment in L-PBF to induce specific phase transitions, such as the precipitation of secondary phases. CET is employed to promote the formation of equiaxed grains through increasing the supercooling capacity. Grain refinement is realized by adding nucleating agents to increase the nucleation sites and promote the equiaxed grain formation.

5.2.1 Phase transition

Due to the layer-by-layer printing nature and the complex thermal cycles during L-PBF, it is feasible to control the phase transition guided by thermodynamic calculation beforehand. Therefore, during alloy design for L-PBF, it is essential to take into account the potential phase transition that may occur during laser processing.

Guo *et al*.[194] proposed a phase-transformation-guided approach for alloy development in the L-PBF of PH17-4 steel. Through controlling scanning parameters, they minimized the formation of δ-ferrite but facilitated the austenitization. Next, they removed the minor alloying elements C, Mn, and Si, which reduced the Ms temperature, to promote the austenite-to-martensite transformation. In the end, UW_17-4 steel was developed with a fully martensitic microstructure at various cooling rates (**Figure 12**). The authors address the importance of understanding the phase transformation dynamics prior to alloy design for AM. Wang *et al*. [195] fabricated 316L with L-PBF and obtained a super combination of yield strength and ductility, breaking the strength-ductility dilemma. It was interpreted that the unique cellular structures, low-angle grain boundaries, and dislocations formed during L-PBF resulted in the high strength, and the work-hardening mechanism contributed to the high elongation.

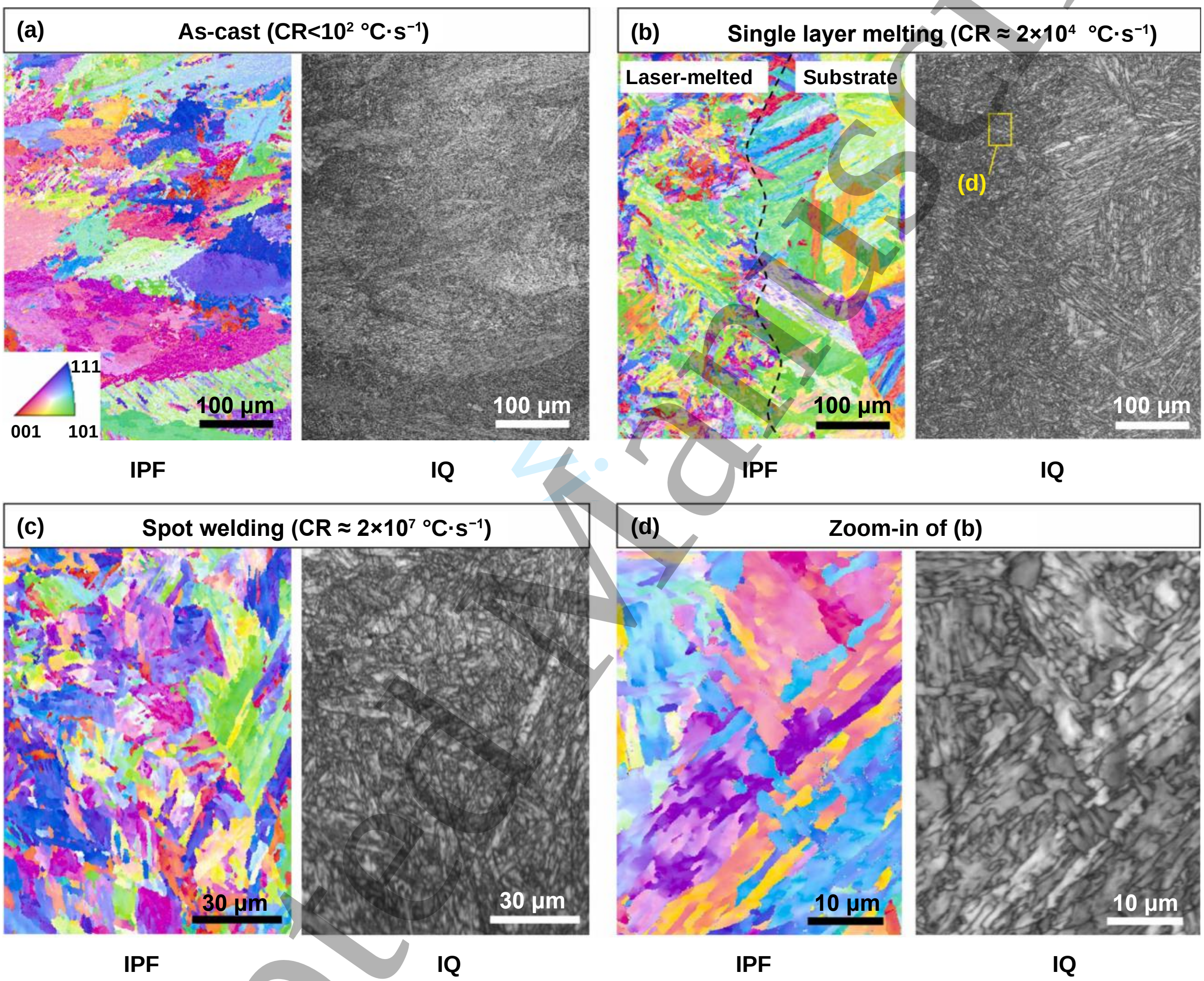

Figure 12. Microstructure of UM_17-4 under different cooling rates. **(a)** EBSD of as-cast UW_17–4 fabricated by arc-melting. The left panel is an inversed pole figure (IPF). The right panel is the corresponding image quality (IQ) map. **(b)** EBSD of UW_17–4 after a single-layer laser melting (transverse cross-section). The substrate is a cast, fully martensitic UW_17–4 after a solution heat treatment. **(c)** EBSD of UW_17–4 after laser spot welding under 156 W laser power with 1 ms laser duration (transverse cross-section). **(d)** EBSD of a zoom-in area from **(b)**. The microstructures for all conditions are fully martensitic. All IPFs share the same color code, which is shown in the inset of **(a)** [194] .

The LPBF-processed alloy is constantly a supersaturated solid solution with a low yield strength and thus requires a post heat treatment. In order to avoid the post processing, in-situ precipitation by optimizing scanning parameters is proposed to induce nano precipitations under the intrinsic heat treatment during AM.

For example, Fe19Ni5Ti steel was tailored for laser additive manufacturing by local control of both nanoprecipitation and martensitic transformation [196]. The as-built steel was hardened in-situ by NiTi nanoprecipitation and it consists of alternating soft (without precipitates) and hard layers (with a high volume fraction of nanoscale precipitates) with a tensile strength of 1.3GPa and 10% elongation.

5.2.2 Columnar-to-equiaxed transition

During L-PBF, if the easy growth direction of crystals is parallel with the thermal gradient, epitaxial growth is facilitated. As a result, columnar grains spanning multiple melt pools are constantly present in the as-built microstructure. Variation in processing parameters during L-PBF determines the temperature gradient and cooling rates, thus affecting the crystal morphology and phase transformation. Although a lot of attempts have been made to promote the columnar-to-equiaxed transition (CET) during L-PBF by optimizing the scanning parameters as shown in **Figure 13** [65], it is still challenging to obtain fully equiaxed grains, particularly for titanium alloys [207]. Therefore, it is significant to design alloys with high CET tendency in order to achieve fully equiaxed grain structures.

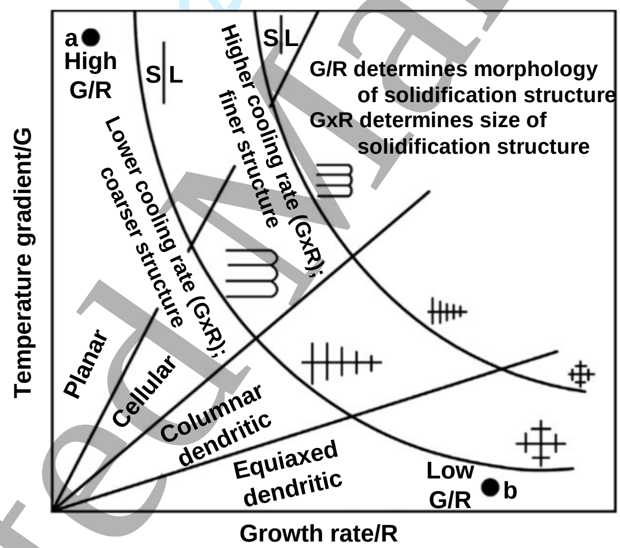

Figure 13. The effect of temperature gradient G and growth rate R on grain size and morphology. S and L stand for solid and liquid, respectively[65].

Mereddy *et al*. [197] added different amounts of carbon to Ti6Al4V during additive manufacturing, and they found that the addition of 0.03 wt.% ~ 0.41 wt.% carbon reduced the prior β grain size and α lath by factors of 5 ~ 6. The carbon segregated at grain boundaries during rapid cooling decreased the solidification temperature, leading to constitutional supercooling. Higher constitutional supercooling capacity thus suppresses the epitaxial growth, leading to a refined microstructure [192]. Gou *et al*. [198] proved that the addition of Nb in Ti6Al4V increased the supercooling capacity, and the planar grain growth mode switched to the cellular grain growth, leading to a refined microstructure. Zhang *et al*. [190] developed Ti-Cu alloys that have a high constitutional supercooling capacity. The as-printed Ti-Cu alloys have a fully equiaxed microstructure without any complex processing parameter control. They demonstrated a pathway to additively manufacture Ti-Cu alloys with fine equiaxed prior-β grains and an ultrafine eutectoid lamellar structure. Similarly, Narayana *et al*. [199] and Simonelli *et al*. [200] investigated the addition of Fe in Ti6Al4V alloy during direct energy deposition and laser powder bed fusion, respectively. They found that the addition of 3% ~ 4% Fe resulted in a significant reduction of prior β grains from ~190 μm to ~70 μm [199] and the further increase of Fe (>4%) content showed only a limited further benefit [200]. Zhang *et al*. [208] found that adding boron to Ti6Al4V resulted in a reduced grain size and refinement of α lath during additive manufacturing. Moreover, grain refinement weakens the texture, reducing the tensile property anisotropy.

5.2.3 Grain refinement

Epitaxial grain growth, prominently prevalent in laser powder bed fusion, is known for the capillary effect and poor strain accommodation capability. Therefore, a lot of efforts have been made to refine grains to prevent hot cracking and enhance the mechanical property isotropy. Adding solute atoms as nuclei to promote equiaxed grain formation has been widely explored in aluminum alloys and titanium alloys [14, 209-211]. However, in nickel-based alloys and steels, the inoculation treatment is not a common practice due to the lack of knowledge of the inoculants [103].

Researchers have attempted to add elements to the standard alloy as inoculants for grain refinement. A successful example is the Scalmalloy, which is developed and patented by the Airbus Group [201]. The introduction of Sc or Zr element to aluminum alloys promotes the formation of a supersaturated solid solution under rapid cooling during L-PBF. The alloy was then strengthened by direct aging to form Al_3Sc or Al_3Zr, which is an $L1_2$ structure and is strongly coherent with the Al matrix [202]. The Al_3X precipitates act as nucleating agents, leading to significant microstructure refinement for the aluminum alloys. The Scalmalloy has both good printability and excellent mechanical properties, i.e., yield strength YS = 520 MPa, ultimate tensile strength UTS = 530 MPa, and elongation = 14% [201]. Due to the success of Scalmalloy with regard to both printability and mechanical properties, similar strategies were explored by other researchers.

Jia *et al.* [203] explored the potential of replacing Sc with Er in the Al-Sc-Zr alloy. They found that the microstructure of the laser remelted Al-Sc-Zr region was mainly composed of fine columnar grains, while the remelted region of Al-Er-Zr alloy consisted of a large-grained structure (**Figure 14**(a)). The Al-Sc-Zr alloy has higher hardness and thermal ability compared with the Al-Er-Zr alloy. Manca *et al*. [204] printed the novel Al-3Ce-7Cu alloy via L-PBF with a low porosity of 0.03%. The mechanical performance is satisfactory with YS = 274 MPa and UTS = 459 MPa at room temperature. The high strength was attributed to the fine Al6.5CeCu6.5 and Al11Ce3 eutectic phase precipitated in the as-built Al-3Ce-7Cu alloy, demonstrating good promise as novel heat-resistant alloys. They also investigated the addition of Cu in the Al-Si-Ni-Fe alloy [205]. The yield compression stress is 355 MPa at 200 °C due to the refined microstructure as a result of Si, $Al_5Fe(Ni,Cu)$ and $Al_3(Ni,Cu)$ phase precipitation (**Figure 14**(b)). Croteau *et al*.[206] designed an Sc-free, age-hardenable aluminum alloy Al-Mg-Zr specifically tailored for L-PBF. The developed Al-Mg-Zr alloy was successfully fabricated via L-PBF without cracks and had an excellent combination of high yield strength (~354 MPa) and high tensile ductility (~20%) after aging due to solid strengthening by Mg in the matrix and the Hall-Petch effect of both sub-micrometer and nano-sized Al_3Zr precipitates. Li *et al*.[123] studied the effect of Zr content on the printability, microstructure evolution, and mechanical properties of Al-Cu-Mg-Mn alloy. With the increase of Zr content from 0 to 4 wt%, the grain size decreased and (**Figure 14**(c)) the yield strength and ultimate tensile stress increased. Nie *et al*. [212] also studied the effect of Zr content on the Al-Cu-Mg-Mn alloy and found that with the increase of Zr content, the grain size decreased first and then tended to be stable (**Figure 14**(c)) while the yield strength and ultimate tensile stress increased first and then decreased.

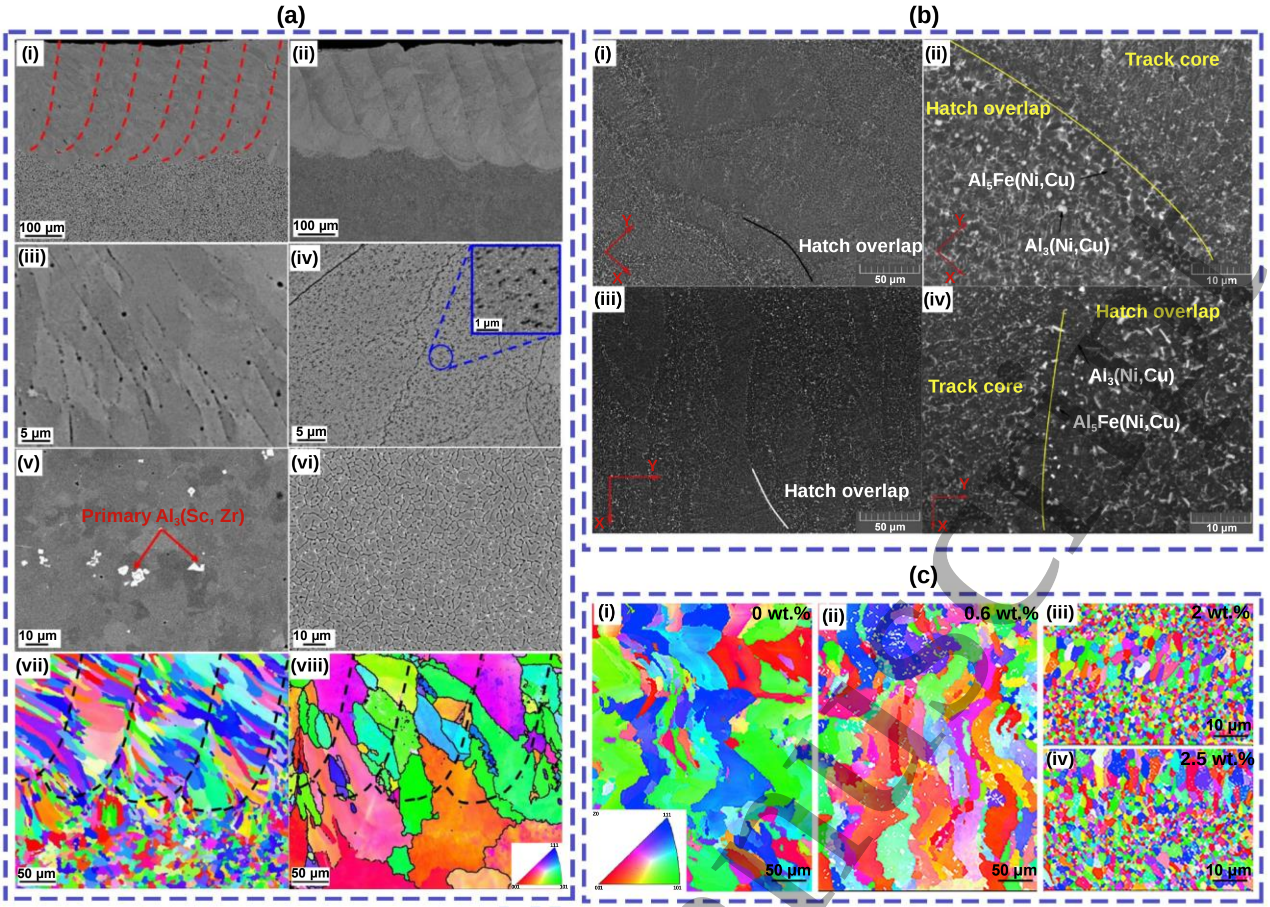

Figure 14. Microstructure refining by adding elements that react with the alloy matrix to form nucleating agents. **(a)** BSE images showing cross section morphologies of **(i)** AlScZr and **(iiii)** AlErZr after laser remelting; microstructures of laser remelted regions of **(iii)** AlScZr and **(iv)** AlErZr; microstructures of casting regions of **(v)** AlScZr and **(vi)** AlErZr. EBSD images of grain morphology on cross sections of laser remelted **(vii)** AlScZr and **(viii)** AlErZr alloys [203]. **(b)** Microstructure of Al-Si-Ni-Fe alloy **(i, ii)** aged for 5 hours at 250°C and annealed for 3 hours at 495°C, and **(iii, iv)** aged for 5 hours at 250°C [205]. **(c)** EBSD maps of Al-4.24Cu-1.97Mg-0.56Mn alloy with different Zr contents, **(i)** 0 wt.%, **(ii)** 0.6 wt.%, **(iii)** 2 wt.%, **(iv)** 2.5 wt.% [212].

In summary, microstructure-oriented strategies are employed to develop alloys tailored for L-PBF in three main ways:

(1) Phase transition-guided approach: this involves leveraging the intrinsic heat treatment during L-PBF to induce specific phase transitions. By utilizing thermodynamic and kinetic software to calculate phase diagrams, the desired phase constitutions are achievable.

(2) Columnar or equiaxed grain structure design: the design of the microstructure focuses on either columnar or equiaxed grain structures, depending on the targeted application. The CET theory is utilized to guide the design by optimizing scanning parameters and controlling the thermal gradient.

(3) Addition of nucleating agents: nucleating agents are added to the alloy to refine the microstructure. This strategy considers the interaction of the nucleating agents with the matrix and their influence on solid solubility and precipitation behavior of other elements in the alloy.

5.3 Machine learning-assisted strategies

In section 5.1 and 5.2, we discussed two primary strategies for alloy design in L-PBF. These strategies rely on a deep understanding of physical mechanisms such as cracking mechanism and phase transitions. In order to accurately design the composition of an alloy with specific properties, validated models or theories are required that can link the composition with defects, microstructure, and properties. Unfortunately, at present, either the cracking mechanism or the phase transition during the complex thermal cycles in L-PBF has not been completely understood. Consequently, a validated correlation between alloy composition and final properties has not been well-established, restricting the alloy development for L-PBF.

In recent years, machine learning (ML), a method to create logistic models from large datasets following specific algorithms, has attracted a lot of attentions in diverse industries. Since ML does not solve complex physical equations based on mechanistic models, the computation is fast and is believed to be capable of making more accurate predictions than human beings [213]. Through learning from the literature data, machine learning enables the prediction of material compositions and properties.

Significant advancements have been achieved in the development of ML-driven metals [88, 214-221]. For instance, Zhang *et al*. [222] successfully employed machine learning to develop four novel Cu-In alloys that possess both high ultimate tensile strength and electrical conductivity (EC). These alloys have the potential to replace costly Cu-Ag alloys currently used in railway wiring. Furthermore, Zhang *et al*. [223] combined feature screening strategy with Bayesian optimization to iteratively design alloys. This approach led to the development of a copper alloy, Cu-1.3Ni-1.4Co-0.56Si-0.03Mg, which exhibits exceptional mechanical and electrical properties. Wang *et al*. [224] proposed a machine learning design system (MLDS) that enables performance-oriented compositional design for complex alloys. The MLDS incorporates machine learning modeling, composition design, and property prediction. Through this system, several high-performance copper alloys were designed, offering an ultimate tensile strength range of 600 ~ 950 MPa and electrical conductivity of 50.0% IACS. To further enhance performance-oriented design, Jiang *et al*. [225] extended the MLDS and successfully designed a new type of aluminum alloy with remarkable ultimate tensile strength (707 ~ 736 MPa) and elongation (7.8% ~ 9.5%). Additionally, Xue *et al*. [226] optimized the composition of Ti-Ni-based shape memory alloy using an active learning strategy and discovered a new alloy, Ti-Ni-Cu-Fe-Pd, with reduced transformation thermal hysteresis (1.84 K).

Successful applications of machine learning in alloy design can also be found in the development of high entropy alloys [227], aluminum alloys [228], and Co-based superalloys [214] that undergo conventional casting or forging processes.

However, the utilization of machine learning in metal additive manufacturing remains limited. Existing literature on ML in the AM field primarily concentrates on optimizing processing parameters [229-231], controlling part geometry [232-234], and detecting defects [234-237]. The incorporation of ML for alloy design specifically for additive manufacturing is notably scarce in current research.

Du *et al*. [218] reduced the defects during L-PBF by combining physical-informed machine learning, mechanistic modeling, and experimental data (**Figure 15**(a)). In order to predict the spheroidizing defect during L-PBF, parameters such as bulk energy density (E), surface tension (F), Marangoni number (M), Richardson number (R), the aspect ratio of the molten pool (ε), and solidification time (T) were taken into account. The spheroidizing sensitivity index was deduced by a genetic algorithm. Two key factors affecting spheroidization were thus found in this way, i.e., Marangoni number and the solidification time of the molten pool. They formulated an equation relating the spheroidizing sensitivity index with the aforementioned six parameters. With this equation, they successfully predicted the spheroidizing defects with an accuracy of 90%. Mondal *et al*. [221] also applied ML in crack prediction, as shown in **Figure 15**(a). Four parameters were used in this ML model, including cooling rate (T), the ratio of the temperature gradient to the solidification growth rate (ε), solidification stress (σ), and the ratio of the vulnerable and relaxation times (β) [221]. The four variables were selected by Pearson correlation analysis. They are independent of each other and can represent the physical characteristics of the cracks [238, 239]. Ultimately, a linear correlation was proposed to calculate the crack sensitivity index (CSI).

Computational alloy design is being widely utilized in various applications. The integration of tools like Thermo-Calc can significantly enhance the efficiency of alloy development. In cases where direct physical predictions are impractical, machine learning methods can be employed to forecast properties based on existing literature data. Multi-objective genetic algorithms are capable of achieving this objective, as shown in **Figure 15**(b). The genetic algorithm is an optimization algorithm that emulates biological evolution processes to iteratively improve solutions to a given problem. The genetic algorithm evolves the chromosomes through genetic operations such as selection, crossover, and mutation. These operations simulate the natural selection process, where individuals with better fitness (i.e., solutions that perform well on the given problem) have a higher probability of being selected for reproduction (**Figure 16**(b)- Genetic algorithm illustration). Dreano *et al*. [217] employed qualitative constraints in their study, aiming to control the fraction of face-centered cubic (FCC) phase within the range of 0.7 ~ 0.94 and ensure that the solidification process starts with the formation of FCC phase. They utilized a genetic algorithm that aimed to minimize the solidification temperature range and maximize the strength index. Alloys meeting all the constraints were evaluated based on their fitness scores. In this way, a crack-free aluminum alloy during L-PBF was designed (**Figure 15**(b)-Al-alloy composition design). Similar methods have also been applied in the design of crack-free austenitic stainless steels for L-PBF (**Figure 15**(b)-Austenitic stainless steel composition design). Sabzi *et al*. [88] defined constraints and goals for the genetic algorithm, including the solidification temperature range, performance index (PI), and the ratio of Cr equivalent to Ni equivalent. They optimized the composition of a 316L alloy and validated its printability. The results demonstrated a significant improvement in the formability of crack-free L-PBF 316L alloy compared to 316L alloys with pores and deformation.

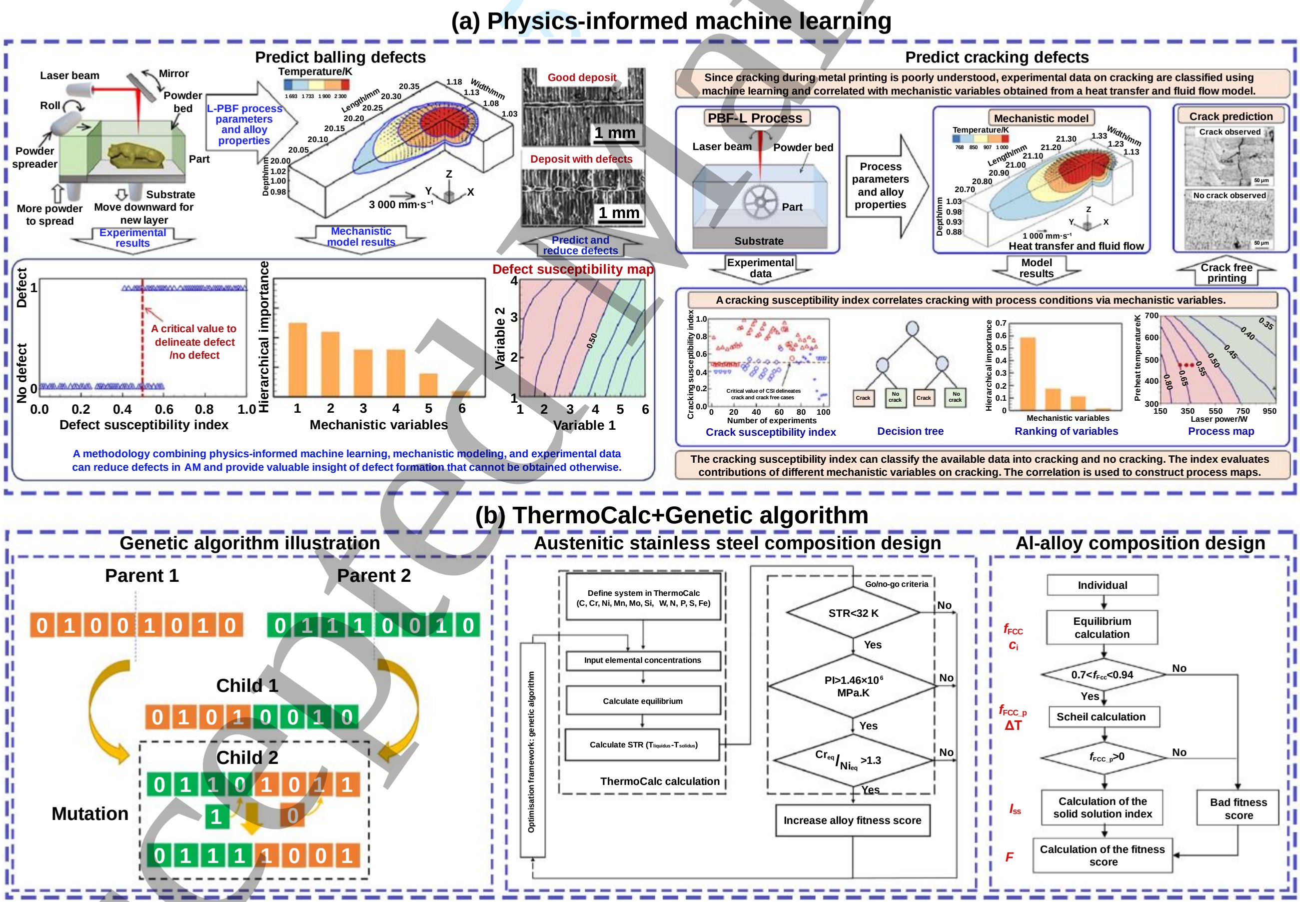

Figure 15. The application of machine learning in printing crack-free alloys in additive manufacturing. (a) Schematic diagram of machine learning model to avoid balling and cracks [218, 221]. (b) Schematic diagram of multi-objective genetic algorithm combined with thermodynamic calculation for designing aluminum alloys and austenitic stainless steels [88, 217].

To summarize, the use of machine learning in alloy design for additive manufacturing is still in its early stages. This is attributed to the lack of an accurate and statistically representative database, which is essential for the prediction accuracy of machine learning. Furthermore, many mechanistic variables of alloys might not be readily available and thus should be calculated based on known data. For instance, temperature gradient, cooling rate, and stresses, which influence the solidification microstructure and cracking, should be calculated by combining CALPHAD-based computational thermodynamic and finite-element-based thermal models. These mechanistic variables are important inputs in the ML model construction.

6. Future outlook and conclusions

Since the emergence of additive manufacturing (AM) in the 1980s, a considerable amount of work on metal additive manufacturing has been published. Despite significant progress in AM, some scientific and technological challenges still need to be addressed. For instance, cracking, anisotropy in building direction, low ductility, and low fatigue resistance constantly occur in additively manufactured alloys, particularly in the LPBF-processed alloys. The previous work has proposed various remedies to tackle these issues during alloy design for L-PBF, as shown in **Figure 16**. However, printable metals with satisfactory mechanical properties represent only a small fraction of commercially available alloys. The following aspects should be emphasized in future research.

(1) The defect formation mechanism in L-PBF requires clarification. Although our understanding of the L-PBF process has significantly advanced (e.g., RGD theory, Kou's criterion), the root cause of cracking during L-PBF has not been completely understood. Due to the complex metallurgical reactions (laser-powder-gas-bulk interactions) during L-PBF, a practical in-situ crack observation technology that can visualize the crack initiation and propagation during L-PBF is in urgent need.

(2) Solidification theories tailored for the L-PBF process need to be developed. The layer-by-layer powder deposition in L-PBF facilitates epitaxial grain growth, which is detrimental to the property isotropy in the final component. Considering the L-PBF process features, a solidification theory accounting for fast cooling, steep temperature gradients, and huge internal stress is required. Additionally, tailored thermodynamic packages that consider the phase transitions during thermal cycles in L-PBF are necessary.

(3) Further exploration of grain boundary segregation engineering is needed during alloy design for L-PBF. Grain boundary manipulation is crucial for the development of crack-resistant alloys, as cracks primarily initiate from grain boundaries. It is important to note that the sub-grain boundary (cell/dendrite) segregation also plays a significant role in crack formation. The enrichment of solute atoms can lead to precipitations, which reduce grain boundary energy and hinder boundary mobility through pinning mechanisms. This pinning effect promotes the formation of equiaxed grains but also introduces stress concentration. Care must be taken when assessing the influence of precipitates on crack sensitivity due to their embrittling nature.

(4) Further research is needed to apply machine learning in alloy design for additive manufacturing, accompanied by the high-quality database. The application of machine learning in alloy design for additive manufacturing is still in its nascent stages. This is primarily due to the limited volume of data available for ML in the additive manufacturing field. Additionally, data consistency in AM is unsatisfactory. For instance, the crack density of a sample can vary significantly when printed with different machines or using different batches of powders. Furthermore, more efforts should be made towards developing physics-informed machine learning models that aid in understanding the cracking and strengthening mechanisms of LPBF-processed alloys.

(5) High-throughput L-PBF equipment or methods are in urgent need, taking into account the time-consuming and costly powder making and conventional L-PBF processes. In-situ alloying presents a high-throughput methodology to design novel alloys for additive manufacturing. By combining multiple elemental powders during printing, engineers can design and test various alloy compositions to achieve desired material properties, reducing the need for pre-alloyed powders that may have limited availability or high costs. By blending elemental powders during printing, the desired alloy composition can be achieved precisely where and when it is needed, providing greater flexibility in material selection. This flexibility in composition enables the rapid exploration of new alloy systems. For instance, blends of titanium and Cr powders have been manufactured using directed energy deposition (DED), and a desirable combination of strength and ductility was obtained [240]. Grigoriev *et al*. mixed Ti, Al, and Nb elemental powders in a turbula mixer and processed the mixture with L-PBF to produce Ti_2AlNb parts [241]. However, incompletely melted and unevenly distributed Nb particles were observed in the printed specimen due to the high melting point of Nb (2 469 °C). Balancing the melting of elements with high melting points while avoiding the evaporation of volatile

elements during parameter optimization remains a challenge in in-situ powder mixing for L-PBF.

This review assessed the printability of four commonly used alloy systems (Fe-, Ni-, Al-, and Ti-based alloys) mainly in laser powder bed fusion additive manufacturing and compared with their weldability. The application of weldability criteria in assessing printability for each alloy was also evaluated. Various pathways for AM alloy design were reviewed and analyzed. The following conclusions were drawn:

(1) The presence of martensite in the as-printed steel microstructure increases crack susceptibility. The Schaeffler diagram can be used to estimate the printability of steels based on their chemistry.

(2) The weldability of nickel-based superalloys does not always align with their printability. The weldability assessment chart, which considers the effects of Ti, Al, Cr, and Co, cannot directly categorize the printability of nickel-based superalloys during L-PBF.

(3) A Pearson correlation map was constructed to identify key factors contributing to cracks in aluminum alloys processed via L-PBF. The map revealed that increasing silicon content and decreasing magnesium content can enhance crack resistance in aluminum alloys during L-PBF.

(4) Titanium alloys generally exhibit less severe cracking during L-PBF. Efforts have been focused on promoting the columnar-to-equiaxed transition during the AM of titanium alloys.

(5) Alloy design strategies for L-PBF can be categorized into three types: 1) crack mitigation-oriented strategies that aim to mitigate cracks through in-depth analysis of the crack formation mechanism, 2) microstructure refining-oriented strategies that focus on synergistically improving crack resistance and mechanical properties by adding alloying elements or nucleation particles, and 3) machine learning-assisted strategies based on AM databases and data analysis.

(6) To accelerate alloy design for L-PBF, there is a need to enhance fundamental understanding of defect formation, building direction anisotropy, low ductility, and low fatigue resistance in LPBF-processed alloys. Thermo-Calc calculations can be utilized to address complex phase transitions during AM by considering features such as extremely fast cooling and cyclic heat treatment. Grain boundary should be carefully manipulated considering the strengthening and embrittling effects of precipitates. In-situ alloying provides a high-throughput method for alloy design, but challenges related to composition homogeneity and melting point variation among elements need to be resolved.

In summary, the complex metallurgical reactions and phase transitions during L-PBF pose challenges to the quality of printed parts. However, they also open avenues for revolutionary alloy design, offering the potential for unprecedented metals with tailored properties in the near future. By addressing the L-PBF processability challenges and exploring innovative alloy design strategies, this review contributes to a better understanding of alloy design for laser powder bed fusion additive manufacturing and guides future research.

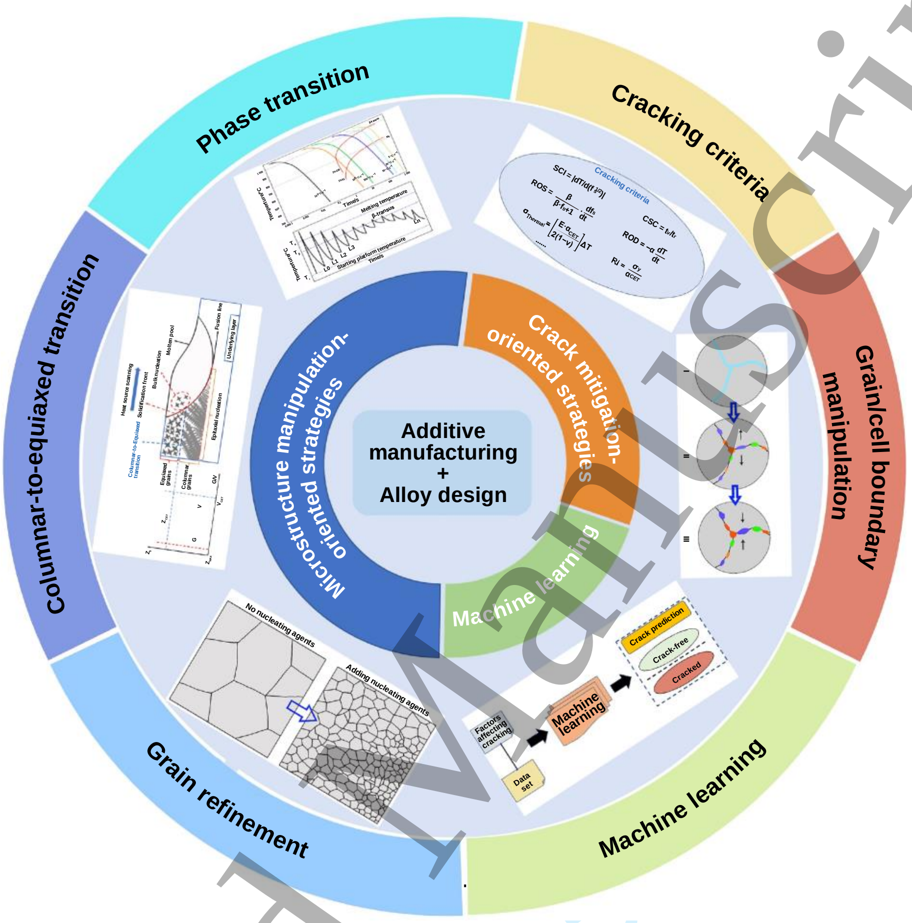

Figure 16. An overview of various alloy design strategies for laser powder bed fusion.

7. Acknowledgments

This study was financially supported by the National Key Research and Development Program of China (2022YFB4600302), National Natural Science Foundation of China (52104368), National Major Science and Technology Projects of China (J2019-VII-0010-0150).

8. References

[1] Sing S L and Yeong W Y 2020 Laser powder bed fusion for metal additive manufacturing: perspectives on recent developments *Virtual Phys. Prototyping.* **15** 359-370

[2] Yin Y, Tan Q, Bermingham M, Mo N, Zhang J and Zhang M-X 2022 Laser additive manufacturing of steels *Int. Mater. Rev.* **67** 487-573

[3] MEINERS WILHELM (DE) W K D D, GASSER ANDRES DR (DE) 1998 Shaped body especially prototype or replacement part production F. G. F. (DE) DE19649865

[4] Li C X, Pisignano D, Zhao Y and Xue J J 2020 Advances in Medical Applications of Additive Manufacturing *Engineering.* **6** 1222-1231

[5] Omiyale B O, Olugbade T O, Abioye T E and Farayibi P K 2022 Wire arc additive manufacturing of aluminium alloys for aerospace and automotive applications: a review *Mater. Sci. Technol.* **38** 391-408

[6] Blakey-Milner B, Gradl P, Snedden G, Brooks M, Pitot J, Lopez E, Leary M, Berto F and du Plessis A 2021 Metal additive manufacturing in aerospace: A review *Mater. Des.* **209** 110008

[7] Gu D D, Shi X Y, Poprawe R, Bourell D L, Setchi R and Zhu J H 2021 Material-structure-performance integrated laser-metal additive manufacturing *Science.* **372** 932abg1487

[8] Shao S, Khonsari M M, Guo S, Meng W J and Li N 2019 Overview: Additive Manufacturing Enabled Accelerated Design of Ni-based Alloys for Improved Fatigue Life *Addit. Manuf.* **29** 100779

[9] Meng L, Zhang W H, Quan D L, Shi G H, Tang L, Hou Y L, Breitkopf P, Zhu J H and Gao T 2020 From Topology Optimization Design to Additive Manufacturing: Today's Success and Tomorrow's Roadmap *Arch. Comput. Methods Eng.* **27** 805-830

[10] Plocher J and Panesar A 2019 Review on design and structural optimisation in additive manufacturing: Towards next-generation lightweight structures *Mater. Des.* **183** 108164

[11] Snow Z, Nassar A R and Reutzel E W 2020 Invited Review Article: Review of the formation and impact of flaws in powder bed fusion additive manufacturing *Addit. Manuf.* **36** 101457

[12] Herzog D, Seyda V, Wycisk E and Emmelmann C 2016 Additive manufacturing of metals *Acta Mater.* **117** 371-392

[13] Wei C, Zhang Z Z, Cheng D X, Sun Z, Zhu M H and Li L 2021 An overview of laser-based multiple metallic material additive manufacturing: from macro- to micro-scales *Int. J. Extreme Manuf.* **3** 012003

[14] Sing S L, Huang S, Goh G D, Goh G L, Tey C F, Tan J H K and Yeong W Y 2021 Emerging metallic systems for additive manufacturing: In-situ alloying and multi-metal processing in laser powder bed fusion *Prog. Mater Sci.* **119** 100795

[15] DebRoy T, Wei H L, Zuback J S, Mukherjee T, Elmer J W, Milewski J O, Beese A M, Wilson-Heid A, De A and Zhang W 2018 Additive manufacturing of metallic components - Process, structure and properties *Prog. Mater Sci.* **92** 112-224

[16] Collins P C, Brice D A, Samimi P, Ghamarian I and Fraser H L 2016 Microstructural Control of Additively Manufactured Metallic Materials **46** 63-91

[17] Tytko D, Choi P-P, Klöwer J, Inden G and Raabe D 2012 Microstructural evolution of a Ni-based superalloy (617B) at 700 °C studied by electron microscopy and atom probe tomography *Acta Materialia.* **60** 1731-1740

[18] Kontis P*et al* 2019 Atomic-scale grain boundary engineering to overcome hot-cracking in additively-manufactured superalloys *Acta Mater.* **177** 209-221

[19] Alipour S, Moridi A, Liou F and Emdadi A 2022 The Trajectory of Additively Manufactured Titanium Alloys with Superior Mechanical Properties and Engineered Microstructures *Addit. Manuf.* **60** 10324

[20] Kotadia H R, Gibbons G, Das A and Howes P D 2021 A review of Laser Powder Bed Fusion Additive Manufacturing of aluminium alloys: Microstructure and properties *Addit. Manuf.* **46** 102155102155

[21] Shamsaei N, Yadollahi A, Bian L K and Thompson S M 2015 An overview overview of Direct Laser Deposition for additive manufacturing; Part II: Mechanical behavior, process parameter optimization and control *Addit. Manuf.* **8** 12-35

[22] Mojumder S, Gan Z T, Li Y F, Al Amin A and Liu W K 2023 Linking process parameters with lack-of-fusion porosity for laser powder bed fusion metal additive manufacturing *Addit. Manuf.* **68** 103500

[23] Galati M and Iuliano L 2018 A literature review of powder-based electron beam melting focusing on numerical simulations *Addit. Manuf.* **19** 1-20

[24] Bayat M, Dong W, Thorborg J, To A C and Hattel J H 2021 A review of multi-scale and multi-physics simulations of metal additive manufacturing processes with focus on modeling strategies *Addit. Manuf.* **47** 102278

[25] Soundararajan B, Sofia D, Barletta D and Poletto M 2021 Review on modeling techniques for powder bed fusion processes based on physical principles *Addit. Manuf.* **47** 102336

[26] Dizon J R C, Espera A H, Chen Q Y and Advincula R C 2018 O Mechanical characterization of 3D-printed polymers *Addit. Manuf.* **20** 44-67

[27] Zhang C, Zhu J K, Zheng H, Li H, Liu S and Cheng G J 2020 A review on microstructures and properties of high entropy alloys manufactured by selective laser melting *Int. J. Extreme Manuf.* **2** 032003

[28] Ojo O O and Taban E 2023 Post-processing treatments-microstructure-performance interrelationship of metal additive manufactured aerospace alloys: a review *Mater. Sci. Technol.* **39** 1-41

[29] Maleki E, Bagherifard S, Bandini M and Guagliano M 2021 Surface post-treatments for metal additive manufacturing: Progress, challenges, and opportunities *Addit. Manuf.* **37** 101619

[30] Mu J R, Sun T T, Leung C L A, Oliveira J P, Wu Y, Wang H W and Wang H Z 2023 Application of electrochemical polishing in surface treatment of additively manufactured structures: A review *Prog. Mater Sci.* **136** 101109

[31] Liu S Y and Shin Y C 2019 Additive manufacturing of Ti6Al4V alloy: A review *Mater. Des.* **164** 107552

[32] Tshephe T S, Akinwamide S O, Olevsky E and Olubambi P A 2022 Additive manufacturing of titanium-based alloys- A review of methods, properties, challenges, and prospects *Heliyon.* **8** e09041

[33] Sing S L 2022 Perspectives on Additive Manufacturing Enabled Beta-Titanium Alloys for Biomedical Applications *International Journal of Bioprinting.* **8** 1-8

[34] Zhang L C and Attar H 2016 Selective Laser Melting of Titanium Alloys and Titanium Matrix Composites for Biomedical Applications: A Review *Adv. Eng. Mater.* **18** 463-475

[35] Zhang L C, Chen L Y, Zhou S F and Luo Z 2023 Powder bed fusion manufacturing of beta-type titanium alloys for biomedical implant applications: A review *J. Alloys Compd.* **936** 168099

[36] Aboulkhair N T, Simonelli M, Parry L, Ashcroft I, Tuck C and Hague R 2019 3D printing of Aluminium alloys: Additive Manufacturing of Aluminium alloys using selective laser melting *Prog. Mater Sci.* **106** 100578

[37] Graybill B, Li M, Malawey D, Ma C, Alvarado-Orozco J M, Martinez-Franco E and Asme 2018 ADDITIVE MANUFACTURING OF NICKEL-BASED SUPERALLOYS 13th ASME International Manufacturing Science and Engineering Conference Coll Stn, TX Jun 18-22 M. E. D. Asme

[38] Mostafaei A*et al* 2023 Additive manufacturing of nickel-based superalloys: A state-of-the-art review on process-structure-defect-property relationship *Prog. Mater Sci.* **136** 101108

[39] Bajaj P, Hariharan A, Kini A, Kurnsteiner P, Raabe D and Jagle E A 2020 Steels in additive manufacturing: A review of their microstructure and properties *Materials Science and Engineering a-Structural Materials Properties Microstructure and Processing.* **772** 138633

[40] Zhu Z, Chen C and Zhang M 2019 Research Progress and Prospect of Laser Additive Manufacturing Technique for Magnesium Alloy *Laser & Optoelectronics Progress.* **56** 1006-4125

[41] Karunakaran R, Ortgies S, Tamayol A, Bobaru F and Sealy M P 2020 Additive manufacturing of magnesium alloys

Bioact. Mater. **5** 44-54

[42] Sun J, Guo M, Shi K and Gu D 2022 Influence of powder morphology on laser absorption behavior and printability of nanoparticle-coated 90W-Ni-Fe powder during laser powder bed fusion *Materials Science in Additive Manufacturing.* **1** 11

[43] Bartolomeu F, Buciumeanu M, Pinto E, Alves N, Carvalho O, Silva F S and Miranda G 2017 316L stainless steel mechanical and tribological behavior-A comparison between selective laser melting, hot pressing and conventional casting *Addit. Manuf.* **16** 81-89

[44] Li Z, Li H, Yin J, Li Y, Nie Z, Li X, You D, Guan K, Duan W and Cao L 2022 A review of spatter in laser powder bed fusion additive manufacturing: In situ detection, generation, effects, and countermeasures *Micromachines.* **13** 1366

[45] Zhang W X, Hou W Y, Deike L and Arnold C 2022 Understanding the Rayleigh instability in humping phenomenon during laser powder bed fusion process *Int. J. Extreme Manuf.* **4** 015201

[46] Wang J S, Fang F Z, An H J, Wu S, Qi H M, Cai Y X and Guo G Y 2023 Laser machining fundamentals: micro, nano, atomic and close-to-atomic scales *Int. J. Extreme Manuf.* **5** 012005

[47] Rashed M G, Bhattacharyya D, Mines R A W, Saadatfar M, Xu A L, Ashraf M, Smith M and Hazell P J 2021 Enhancing the bond strength in the meta-crystal lattice of architected materials by harnessing the non-equilibrium solidification in metal additive manufacturing *Addit. Manuf.* **37** 101682

[48] Sun Z, Guo W and Li L 2020 Numerical modelling of heat transfer, mass transport and microstructure formation in a high deposition rate laser directed energy deposition process *Addit. Manuf.* **33** 101175

[49] Vilaro T, Colin C, Bartout J D, Naze L and Sennour M 2012 Microstructural and mechanical approaches of the selective laser melting process applied to a nickel-base superalloy *Materials Science and Engineering a-Structural Materials Properties Microstructure and Processing.* **534** 446-451

[50] Liu F, Lin X, Song M, Zhao W, Chen J and Huang W 2011 Effect of intermediate heat treatment temperature on microstructure and notch sensitivity of laser solid formed Inconel 718 superalloy *Journal of Wuhan University of Technology-Mater. Sci. Ed.* **26** 908-913

[51] Chlebus E, Gruber K, Kuźnicka B, Kurzac J and Kurzynowski T 2015 Effect of heat treatment on the microstructure and mechanical properties of Inconel 718 processed by selective laser melting *Materials Science Engineering: A.* **639** 647-655

[52] Khairallah S A, Anderson A T, Rubenchik A and King W E 2016 Laser powder-bed fusion additive manufacturing: Physics of complex melt flow and formation mechanisms of pores, spatter, and denudation zones *Acta Mater.* **108** 36-45

[53] Zhang T, Huang Z, Yang T, Kong H, Luan J, Wang A, Wang D, Kuo W, Wang Y and Liu C-T 2021 In situ design of advanced titanium alloy with concentration modulations by additive manufacturing *Science.* **374** 478-482

[54] Zhang F, Levine L E, Allen A J, Stoudt M R, Lindwall G, Lass E A, Williams M E, Idell Y and Campbell C E 2018 Effect of heat treatment on the microstructural evolution of a nickel-based superalloy additive-manufactured by laser powder bed fusion *Acta Mater.* **152** 200-214

[55] Bartlett J L and Li X D 2019 An overview of residual stresses in metal powder bed fusion *Addit. Manuf.* **27** 131-149

[56] Zhang J L, Gao J B, Song B, Zhang L J, Han C J, Cai C, Zhou K and Shi Y S 2021 A novel crack-free Ti-modified Al-Cu-Mg alloy designed for selective laser melting *Addit. Manuf.* **38** 101829

[57] Yadollahi A, Shamsaei N, Thompson S M, Elwany A and Bian L 2017 Effects of building orientation and heat treatment on fatigue behavior of selective laser melted 17-4 PH stainless steel *Int. J. Fatigue.* **94** 218-235

[58] Panwisawas C, Tang Y B T and Reed R C 2020 Metal 3D printing as a disruptive technology for superalloys *Nat.*

Commun. **11** 2327

[59] Qu M, Guo Q, Escano L I, Nabaa A, Hojjatzadeh S M H, Young Z A and Chen L J N c 2022 Controlling process instability for defect lean metal additive manufacturing **13** 1-8

[60] Carter L N, Attallah M M and Reed R C 2012 Laser Powder Bed Fabrication of Nickel-Base Superalloys: Influence of Parameters; Characterisation, Quantification and Mitigation of Cracking 12th International Symposium on Superalloys Seven Springs, PA Sep 09-13 Tms, S. M. Univ Birmingham and B. B. T. T. W. M. E. Mat

[61] Wang N, Mokadem S, Rappaz M and Kurz W 2004 Solidification cracking of superalloy single- and bi-crystals *Acta Mater.* **52** 3173-3182

[62] Farup I and Mo A 2000 Two-phase modeling of mushy zone parameters associated with hot tearing *Metallurgical and Materials Transactions A.* **31** 1461-1472

[63] Xu J H, Kontis P, Peng R L and Moverare J 2022 Modelling of additive manufacturability of nickel-based superalloys for laser powder bed fusion *Acta Mater.* **240** 118307

[64] Fu J, Li H, Song X and Fu M W 2022 Multi-scale defects in powder-based additively manufactured metals and alloys *Journal of Materials Science & Technology.* **122** 165-199

[65] Kou S 2003 New Jersey, USA Welding metallurgy **431** 223-225

[66] Ramirez A J and Lippold J C 2004 High temperature behavior of Ni-base weld metal - Part I. Ductility and microstructural characterization *Materials Science and Engineering a-Structural Materials Properties Microstructure and Processing.* **380** 259-271

[67] Ramirez A J and Lippold J C 2004 High temperature behavior of Ni-base weld metal - Part II - Insight into the mechanism for ductility dip cracking *Materials Science and Engineering a-Structural Materials Properties Microstructure and Processing.* **380** 245-258

[68] Noecker F F and DuPont J N 2009 Metallurgical Investigation into Ductility Dip Cracking in Ni-Based Alloys: Part II *Welding J.* **88** 62S-77S

[69] Martin J H, Yahata B D, Hundley J M, Mayer J A, Schaedler T A and Pollock T M 2017 3D printing of high-strength aluminium alloys *Nature.* **549** 365-369

[70] Vrancken B, Thijs L, Kruth J P and Van Humbeeck J 2014 Microstructure and mechanical properties of a novel β titanium metallic composite by selective laser melting *Acta Materialia.* **68** 150-158

[71] Zhang T and Liu C-T 2022 Design of titanium alloys by additive manufacturing: A critical review *Advanced Powder Materials.* **1** 100014

[72] Tang Y B T, Panwisawas C, Ghoussoub J N, Gong Y L, Clark J W G, Nemeth A A N, McCartney D G and Reed R C 2021 Alloys-by-design: Application to new superalloys for additive manufacturing *Acta Mater.* **202** 417-436

[73] Zhang H Z, Xu M T, Liu Z D, Li C Y, Kumar P, Liu Z H and Zhang Y M 2021 Microstructure, surface quality, residual stress, fatigue behavior and damage mechanisms of selective laser melted 304L stainless steel considering building direction *Addit. Manuf.* **46** 102147

[74] Ghayoor M, Lee K, He Y J, Chang C H, Paul B K and Pasebani S 2020 Selective laser melting of 304L stainless steel: Role of volumetric energy density on the microstructure, texture and mechanical properties *Addit. Manuf.* **32** 101011

[75] Wilson-Heid A E and Beese A M 2021 Combined effects of porosity and stress state on the failure behavior of laser powder bed fusion stainless steel 316L *Addit. Manuf.* **39** 101862

[76] Karthik G M, Kim E S, Sathiyamoorthi P, Zargaran A, Jeong S G, Xiong R, Kang S H, Cho J W and Kim H S 2021 Delayed deformation-induced martensite transformation and enhanced cryogenic tensile properties in laser additive manufactured 316L austenitic stainless steel *Addit. Manuf.* **47** 102314

[77] Sabooni S, Chabok A, Feng S C, Blaauw H, Pijper T C, Yang H J and Pei Y T 2021 Laser powder bed fusion of 17-4

PH stainless steel: A comparative study on the effect of heat treatment on the microstructure evolution and mechanical properties *Additive Manufacturing.* **46** 102176

[78] Leo P, D'Ostuni S, Perulli P, Sastre M A C, Fernández-Abia A I and Barreiro J 2019 Analysis of microstructure and defects in 17-4 PH stainless steel sample manufactured by Selective Laser Melting *Procedia Manuf.* **41** 66-73

[79] Wang L, Dong C F, Kong D C, Man C, Liang J X, Wang C J, Xiao K and Li X G 2020 Effect of Manufacturing Parameters on the Mechanical and Corrosion Behavior of Selective Laser-Melted 15-5PH Stainless Steel *Steel Res. Int.* **91** 1900447

[80] Nong X D and Zhou X L 2021 Effect of scanning strategy on the microstructure, texture, and mechanical properties of 15-5PH stainless steel processed by selective laser melting *Mater. Charact.* **174** 111012

[81] Saby Q, Buffiere J Y, Maire E, Joffre T, Bajolet J, Garabedian S, Vikner P and Boulnat X 2021 Laser Powder Bed Fusion printability of cobalt-free steel powders for manufacturing injection molds *Addit. Manuf.* **44** 102031

[82] Mazur M, Brincat P, Leary M and Brandt M 2017 Numerical and experimental evaluation of a conformally cooled H13 steel injection mould manufactured with selective laser melting *Int. J. Adv. Manuf. Technol.* **93** 881-900

[83] Mutua J, Nakata S, Onda T and Chen Z C 2018 Optimization of selective laser melting parameters and influence of post heat treatment on microstructure and mechanical properties of maraging steel *Mater. Des.* **139** 486-497

[84] Mei X Y, Yan Y, Fu H D, Gao X D, Huang S Y and Qiao L J 2022 Effect of aging temperature on microstructure evolution and strengthening behavior of L-PBF 18Ni(300) maraging steel *Addit. Manuf.* **58** 103071

[85] Zhao X, Wei Q S, Song B, Liu Y, Luo X W, Wen S F and Shi Y S 2015 Fabrication and Characterization of AISI 420 Stainless Steel Using Selective Laser Melting *Materials and Manufacturing Processes.* **30** 1283-1289

[86] Narasimharaju S R, Zeng W H, See T L, Zhu Z C, Scott P, J. X and Lou S 2022 A comprehensive review on laser powder bed fusion of steels: Processing, microstructure, defects and control methods, mechanical properties, current challenges and future trends *J. Manuf. Processes.* **75** 375-414

[87] Alhassan M and Bashiru Y 2021 Carbon Equivalent Fundamentals in Evaluating the Weldability of Microalloy and Low Alloy Steels *World Journal of Engineering Technology.* **9** 782-792

[88] Sabzi H E, Maeng S, Liang X Z, Simonelli M, Aboulkhair N T and Rivera-Diaz-del-Castillo P E J 2020 Controlling crack formation and porosity in laser powder bed fusion: Alloy design and process optimisation *Addit. Manuf.* **34** 101360

[89] Kim K S, Kim Y K and Lee K A 2022 Effect of repeated laser scanning on the microstructure evolution of carbon-bearing martensitic steel manufactured by laser powder bed fusion: Quenching-partitioning drives carbon-stabilized austenite formation *Addit. Manuf.* **60** 103262

[90] Rajasekhar A 2015 Effect of welding process and post weld heat treatments on microstructure and mechanical properties of AISI 431 martensitic stainless steel *Int J Tech Res Appl.* **3** 280-285

[91] Liu Y, Li A, Cheng X, Zhang S and Wang H 2016 Effects of heat treatment on microstructure and tensile properties of laser melting deposited AISI 431 martensitic stainless steel *Materials Science Engineering: A.* **666** 27-33

[92] Stoll P, Spierings A, Wegener K, Polster S and Gebauer M 2016 SLM processing of 14 Ni (200 Grade) maraging steel DDMC 2016: Proceedings of the 3rd Fraunhofer Direct Digital Manufacturing Conference

[93] Kose C 2021 Dissimilar Laser Beam Welding of AISI 420 Martensitic Stainless Steel to AISI 2205 Duplex Stainless Steel: Effect of Post-Weld Heat Treatment on Microstructure and Mechanical Properties *J. Mater. Eng. Perform.* **30** 7417-7448

[94] Geenen K, Rottger A, Feld F and Theisen W 2019 Microstructure, mechanical, and tribological properties of M3:2 high-speed steel processed by selective laser melting, hot-isostatic pressing, and casting *Addit. Manuf.* **28**

585-599

[95] Yan J J, Zhou Y H, Gu R N, Zhang X M, Quach W M and Yan M 2019 A Comprehensive Study of Steel Powders (316L, H13, P20 and 18Ni300) for Their Selective Laser Melting Additive Manufacturing *Metals.* **9** 86

[96] Guo P, Zou B, Huang C Z and Gao H B 2017 Study on microstructure, mechanical properties and machinability of efficiently additive manufactured AISI 316L stainless steel by high-power direct laser deposition *J. Mater. Process. Technol.* **240** 12-22

[97] Proebstle M, Neumeier S, Hopfenmueller J, Freund L P, Niendorf T, Schwarze D and Goeken M 2016 Superior creep strength of a nickel-based superalloy produced by selective laser melting *Materials Science and Engineering a-Structural Materials Properties Microstructure and Processing.* **674** 299-307

[98] Volpato G M, Tetzlaff U and Fredel M C 2022 A comprehensive literature review on laser powder bed fusion of Inconel superalloys *Addit. Manuf.* **55** 102871

[99] https://3dprintingindustry.com/news/ge-aviation-celebrates-30000th-3d-printed-fuel-nozzle-141165/

[100] Catchpole-Smith S, Aboulkhair N, Parry L, Tuck C, Ashcroft I A and Clare A 2017 Fractal scan strategies for selective laser melting of 'unweldable' nickel superalloys *Additive Manufacturing.* **15** 113-122

[101] Haafkens M and Matthey J H 1982 A new approach to the weldability of nickel-base As-cast and power metallurgy superalloys *Weld. J.* **61** 11

[102] Tomus D, Rometsch P A, Heilmaier M and Wu X H 2017 Effect of minor alloying elements on crack-formation characteristics of Hastelloy-X manufactured by selective laser melting *Addit. Manuf.* **16** 65-72

[103] Zhao Y A, Ma Z Q, Yu L M and Liu Y C 2023 New alloy design approach to inhibiting hot cracking in laser additive manufactured nickel-based superalloys *Acta Mater.* **247** 118736

[104] Markanday J 2022 Applications of alloy design to cracking resistance of additively manufactured Ni-based alloys *Materials Science Technology.* **6** 1-15

[105] Gotelid S, Ma T R, Lyphout C, Vang J, Stalnacke E, Holmberg J, Hosseini S and Strondl A 2021 Effect of post-processing on microstructure and mechanical properties of Alloy 718 fabricated using powder bed fusion additive manufacturing processes *Rapid Prototyping J.* **27** 1617-1632

[106] Javidrad H R and Salemi S 2020 Effect of the Volume Energy Density and Heat Treatment on the Defect, Microstructure, and Hardness of L-PBF Inconel 625 *Metallurgical and Materials Transactions a-Physical Metallurgy and Materials Science.* **51** 5880-5891

[107] Zhou W Z, Tian Y S, Tan Q B, Qiao S, Luo H, Zhu G L, Shu D and Sun B D 2022 Effect of carbon content on the microstructure, tensile properties and cracking susceptibility of IN738 superalloy processed by laser powder bed fusion *Addit. Manuf.* **58** 103016

[108] Christofidou K, Pang H, Li W, Pardhi Y, Jones C, Jones N and Stone H 2020 Microstructural control and optimization of Haynes 282 manufactured through laser powder bed fusion Superalloys 2020: Proceedings of the 14th International Symposium on Superalloys

[109] Bauer T, Dawson K, Spierings A B and Wegener K 2015 Microstructure and mechanical characterisation of SLM processed Haynes® 230® Proceedings of the 26th annual international solid freeform fabrication symposium

[110] Zhang L, Li Y T, Zhang S and Zhang Q D 2021 Selective laser melting of IN738 superalloy with a low Mn plus Si content: Effect of energy input on characteristics of molten pool, metallurgical defects, microstructures and mechanical properties *Materials Science and Engineering a-Structural Materials Properties Microstructure and Processing.* **826** 141985

[111] Marchese G, Parizia S, Saboori A, Manfredi D, Lombardi M, Fino P, Ugues D and Biamino S 2020 The Influence of the Process Parameters on the Densification and Microstructure Development of Laser Powder Bed Fused Inconel 939 *Metals.* **10** 882

[112] Sanchez-Mata O, Wang X L, Muniz-Lerma J A, Shandiz M A, Gauvin R and Brochu M 2018 Fabrication of Crack-Free Nickel-Based Superalloy Considered Non-Weldable during Laser Powder Bed Fusion *Materials.* **11** 1288

[113] Chakraborty A, Tangestani R, Muhammad W, Sabiston T, Masse J-P, Batmaz R, Wessman A and Martin É 2022 Micro-cracking mechanism of RENÉ 108 thin-wall components built by laser powder bed fusion additive manufacturing *Mater. Today Commun.* **30** 103139

[114] Peng K, Duan R, Liu Z, Lv X, Li Q, Zhao F, Wei B, Nong B and Wei S J M 2020 Cracking behavior of rené 104 Nickel-based superalloy prepared by selective laser melting using different scanning strategies **13** 2149

[115] Carter L N, Wang X, Read N, Khan R, Aristizabal M, Essa K and Attallah M M 2016 Process optimisation of selective laser melting using energy density model for nickel based superalloys *Mater. Sci. Technol.* **32** 657-661

[116] Ghoussoub J N, Tang Y T, Dick-Cleland W J B, Nemeth A A N, Gong Y L, McCartney D G, Cocks A C F and Reed R C 2022 On the Influence of Alloy Composition on the Additive Manufacturability of Ni-Based Superalloys *Metallurgical and Materials Transactions a-Physical Metallurgy and Materials Science.* **53** 962-983

[117] Chen Z, Chen S G, Wei Z Y, Zhang L J, Wei P, Lu B H, Zhang S Z and Xiang Y 2018 Anisotropy of nickel-based superalloy K418 fabricated by selective laser melting *Progress in Natural Science-Materials International.* **28** 496-504

[118] Asgari H, Baxter C, Hosseinkhani K and Mohammadi M 2017 On microstructure and mechanical properties of additively manufactured AlSi10Mg_200C using recycled powder *Materials Science and Engineering: A.* **707** 148-158

[119] Buchbinder D, Schleifenbaum H, Heidrich S, Meiners W and Bültmann J 2011 High Power Selective Laser Melting (HP SLM) of Aluminum Parts *Physics Procedia.* **12** 271-278

[120] Stopyra W, Gruber K, Smolina I, Kurzynowski T and Kuznicka B 2020 Laser powder bed fusion of AA7075 alloy: Influence of process parameters on porosity and hot cracking *Addit. Manuf.* **35** 101270

[121] Li G 2022 Development of High Strength Aluminum-Based Alloys for Laser Powder Bed Fusion: *[D]. KU Leuven: Belgium*

[122] Hauser T, Reisch R T, Breese P P, Lutz B S, Pantano M, Nalam Y, Bela K, Kamps T, Volpp J and Kaplan A F H 2021 Porosity in wire arc additive manufacturing of aluminium alloys *Addit. Manuf.* **41** 101993

[123] Li G C, Brodu E, Soete J, Wei H L, Liu T T, Yang T, Liao W H and Vanmeensel K 2021 Exploiting the rapid solidification potential of laser powder bed fusion in high strength and crack-free Al-Cu-Mg-Mn-Zr alloys *Addit. Manuf.* **47** 102210

[124] Mathers G 2002 The welding of aluminium and its alloys: a volume in woodhead publishing series in welding and other joining technologies. (Woodhead, Cambridge)

[125] Opprecht M, Garandet J P, Roux G, Flament C and Soulier M 2020 A solution to the hot cracking problem for aluminium alloys manufactured by laser beam melting *Acta Mater.* **197** 40-53

[126] Tonelli L, Laghi V, Palermo M, Trombetti T and Ceschini L 2021 AA5083 (Al–Mg) plates produced by wire-and-arc additive manufacturing: Effect of specimen orientation on microstructure and tensile properties *Progress in Additive Manufacturing.* **6** 479-494

[127] Zhou L, Hyer H, Park S, Pan H, Bai Y L, Rice K P and Sohn Y 2019 Microstructure and mechanical properties of Zr-modified aluminum alloy 5083 manufactured by laser powder bed fusion *Addit. Manuf.* **28** 485-496

[128] Zhang H, Zhu H H, Qi T, Hu Z H and Zeng X Y 2016 Selective laser melting of high strength Al-Cu-Mg alloys: Processing, microstructure and mechanical properties *Materials Science and Engineering a-Structural Materials Properties Microstructure and Processing.* **656** 47-54

[129] Kimura T, Nakamoto T, Ozaki T and Miki T 2021 Microstructures and mechanical properties of aluminum-

transition metal binary alloys (Al-Fe, Al-Mn, and Al-Cr) processed by laser powder bed fusion *J. Alloys Compd.* **872** 159680

[130] Zhao L, Song L B, Macias J G S, Zhu Y X, Huang M S, Simar A and Li Z H 2022 Review on the correlation between microstructure and mechanical performance for laser powder bed fusion AlSi10Mg *Addit. Manuf.* **56** 102914

[131] Kou S 2015 A criterion for cracking during solidification *Acta Materialia.* **88** 366-374

[132] Flemings M C 1974 Solidification processing *Metallurgical Materials Transactions B.* **5** 2121-2134

[133] Hyer H, Zhou L, Mehta A, Park S, Huynh T, Song S T, Bai Y L, Cho K, McWilliams B and Sohn Y 2021 Composition-dependent solidification cracking of aluminum-silicon alloys during laser powder bed fusion *Acta Mater.* **208** 116698

[134] Li R, Wang M, Li Z, Cao P, Yuan T and Zhu H 2020 Developing a high-strength Al-Mg-Si-Sc-Zr alloy for selective laser melting: Crack-inhibiting and multiple strengthening mechanisms *Acta Materialia.* **193** 83-98

[135] Khan K, Mohan L S, De A and DebRoy T 2022 Rapid calculation of part scale residual stress-Powder bed fusion of stainless steel, and aluminum, titanium, nickel alloys *Addit. Manuf.* **60** 103240

[136] Galy C, Le Guen E, Lacoste E and Arvieu C 2018 Main defects observed in aluminum alloy parts produced by SLM: From causes to consequences *Addit. Manuf.* **22** 165-175

[137] Bartkowiak K, Ullrich S, Frick T and Schmidt M 2011 New Developments of Laser Processing Aluminium Alloys via Additive Manufacturing Technique 6th International WLT Conference on Lasers in Manufacturing (LiM) Munich, GERMANY May 23-26 S. German Sci Laser

[138] Karg M, Ahuja B, Kuryntsev S, Gorunov A and Schmidt M 2014 Processability of high strength Aluminum-Copper alloys AW-2022 and 2024 by Laser Beam Melting in Powder Bed 2014 International Solid Freeform Fabrication Symposium

[139] Rees D T, Leung C L A, Elambasseril J, Marussi S, Shah S, Marathe S, Brandt M, Easton M and Lee P D 2023 In situ X-ray imaging of hot cracking and porosity during LPBF of Al-2139 with TiB2 additions and varied process parameters *Materials Design.* 112031

[140] Wu S B, Lei Z L, Li B W, Liang J W and Chen Y B 2022 Hot cracking evolution and formation mechanism in 2195 Al-Li alloy printed by laser powder bed fusion *Addit. Manuf.* **54** 102762

[141] Karg M C H, Ahuja B, Wiesenmayer S, Kuryntsev S V and Schmidt M 2017 Effects of process conditions on the mechanical behavior of aluminium wrought alloy EN AW-2219 (AlCu6Mn) additively manufactured by laser beam melting in powder bed *Micromachines.* **8** 23

[142] Casati R, Lemke J, Alarcon A and Vedani M 2017 Aging Behavior of High-Strength Al Alloy 2618 Produced by Selective Laser Melting *Metallurgical and Materials Transactions a-Physical Metallurgy and Materials Science.* **48A** 575-579

[143] Wang P, Gammer C, Brenne F, Prashanth K G, Mendes R G, Rummeli M H, Gemming T, Eckert J and Scudino S 2018 Microstructure and mechanical properties of a heat-treatable Al-3.5Cu-1.5Mg-1Si alloy produced by selective laser melting *Materials Science and Engineering a-Structural Materials Properties Microstructure and Processing.* **711** 562-570

[144] Qi Y, Hu Z H, Zhang H, Nie X J, Zhang C C and Zhu H H 2021 High strength Al-Li alloy development for laser powder bed fusion *Addit. Manuf.* **47** 102249

[145] Qi X, Takata N, Suzuki A, Kobashi M and Kato M 2020 Laser powder bed fusion of a near-eutectic Al-Fe binary alloy: Processing and microstructure *Addit. Manuf.* **35** 101308

[146] Kimura T and Nakamoto T 2016 Microstructures and mechanical properties of A356 (AlSi7Mg0.3) aluminum alloy fabricated by selective laser melting *Mater. Des.* **89** 1294-1301

[147] Rao H, Giet S, Yang K, Wu X H and Davies C H J 2016 The influence of processing parameters on aluminium alloy

A357 manufactured by Selective Laser Melting *Mater. Des.* **109** 334-346

[148] Vanzetti M, Virgillito E, Aversa A, Manfredi D, Bondioli F, Lombardi M and Fino P 2021 Short Heat Treatments for the F357 Aluminum Alloy Processed by Laser Powder Bed Fusion *Materials.* **14** 6157

[149] Pereira J C, Gil E, Solaberrieta L, San Sebastian M, Bilbao Y and Rodriguez P P 2020 Comparison of AlSi7Mg0.6 alloy obtained by selective laser melting and investment casting processes: Microstructure and mechanical properties in as-built/as-cast and heat-treated conditions *Materials Science and Engineering a-Structural Materials Properties Microstructure and Processing.* **778** 139124

[150] Read N, Wang W, Essa K and Attallah M M 2015 Selective laser melting of AlSi10Mg alloy: Process optimisation and mechanical properties development *Mater. Des.* **65** 417-424

[151] Kimura T, Nakamoto T, Mizuno M and Araki H 2017 Effect of silicon content on densification, mechanical and thermal properties of Al-xSi binary alloys fabricated using selective laser melting *Materials Science and Engineering a-Structural Materials Properties Microstructure and Processing.* **682** 593-602

[152] Olakanmi E O 2013 Selective laser sintering/melting (SLS/SLM) of pure Al, Al-Mg, and Al-Si powders: Effect of processing conditions and powder properties *J. Mater. Process. Technol.* **213** 1387-1405

[153] Mehta A*et al* 2021 Additive manufacturing and mechanical properties of the dense and crack free Zr-modified aluminum alloy 6061 fabricated by the laser-powder bed fusion *Addit. Manuf.* **41** 101966

[154] Li F, Li Z C, Tang C L, Zhang L J, Tan Q Y, Chen C, Zhang M X and Zhou K C 2023 Design high-strength Al-Mg-Si alloy fabricated by laser powder bed fusion: Cracking suppression and strengthening mechanism *Materials Science and Engineering a-Structural Materials Properties Microstructure and Processing.* **864** 144591

[155] Riener K, Pfalz T, Funcke F and Leichtfried G 2022 Processability of high-strength aluminum 6182 series alloy via laser powder bed fusion (LPBF) *Int. J. Adv. Manuf. Technol.* **119** 4963-4977

[156] Montero-Sistiaga M L, Mertens R, Vrancken B, Wang X, Van Hooreweder B, Kruth J-P and Van Humbeeck J 2016 Changing the alloy composition of Al7075 for better processability by selective laser melting *J. Mater. Process. Technol.* **238** 437-445

[157] Yang Y, Li M and Li K 2014 Comparison and analysis of main effect elements of machining distortion for aluminum alloy and titanium alloy aircraft monolithic component *The International Journal of Advanced Manufacturing Technology.* **70** 1803-1811

[158] Tao Q Y*et al* 2020 Selective laser melting of CP-Ti to overcome the low cost and high performance trade-off *Addit. Manuf.* **34** 101198

[159] Lu S*et al* 2023 Tailoring hierarchical microstructures to improve the strength and plasticity of a laser powder bed fusion additively manufactured Ti-6Al-4V alloy *Addit. Manuf.* **71** 103603

[160] Wang L Y, Song Z, Zhang X, Park J S, Almer J, Zhu G M, Chen Y W, Li Q, Zeng X Q and Li Y J 2022 Developing ductile and isotropic Ti alloy with tailored composition for laser powder bed fusion *Addit. Manuf.* **52** 102656

[161] Chen M, Van Petegem S, Zou Z Y, Simonelli M, Tse Y Y, Chang C S T, Makowska M G, Sanchez D F and Swygenhoven H M V 2022 Microstructural engineering of a dual-phase Ti-Al-V-Fe alloy via in situ alloying during laser powder bed fusion *Addit. Manuf.* **59** 103173

[162] Oh S A*et al* 2021 High speed synchrotron X-ray diffraction experiments resolve microstructure and phase transformation in laser processed Ti-6Al-4V *Mater. Res. Lett.* **9** 429-436

[163] Scibior A, Pietrzyk L, Plewa Z and Skiba A 2020 Vanadium: Risks and possible benefits in the light of a comprehensive overview of its pharmacotoxicological mechanisms and multi-applications with a summary of further research trends *J. Trace Elem. Med. Biol.* **61** 126508

[164] Issariyapat A, Huang J, Teramae T, Kariya S, Bahador A, Visuttipitukul P, Umeda J, Alhazaa A and Kondoh K 2023 Microstructure Refinement and Strengthening Mechanisms of Additively Manufactured Ti-Zr Alloys

Prepared From Pre-mixed Feedstock *Addit. Manuf.* 103649

[165] Chlebus E, Kuznicka B, Kurzynowski T and Dybala B 2011 Microstructure and mechanical behaviour of Ti-6Al-7Nb alloy produced by selective laser melting *Mater. Charact.* **62** 488-495

[166] Geetha M, Singh A K, Asokamani R and Gogia A K 2009 Ti based biomaterials, the ultimate choice for orthopaedic implants - A review *Prog. Mater Sci.* **54** 397-425

[167] Bandyopadhyay A, Espana F, Balla V K, Bose S, Ohgami Y and Davies N M 2010 Influence of porosity on mechanical properties and in vivo response of Ti6Al4V implants *Acta Biomater.* **6** 1640-1648

[168] Li Y J, Li X P, Zhang L C and Sercombe T B 2015 Processing and properties of topologically optimised biomedical Ti-24Nb-4Zr-8Sn scaffolds manufactured by selective laser melting *Materials Science and Engineering a-Structural Materials Properties Microstructure and Processing.* **642** 268-278

[169] Niinomi M 2008 Mechanical biocompatibilities of titanium alloys for biomedical applications *J. Mech. Behav. Biomed. Mater.* **1** 30-42

[170] Cain V, Thijs L, Van Humbeeck J, Van Hooreweder B and Knutsen R 2015 Crack propagation and fracture toughness of Ti6A14V alloy produced by selective laser melting *Addit. Manuf.* **5** 68-76

[171] Colombo-Pulgarin J C, Biffi C A, Vedani M, Celentano D, Sanchez-Egea A, Boccardo A D and Ponthot J P 2021 Beta Titanium Alloys Processed By Laser Powder Bed Fusion: A Review *J. Mater. Eng. Perform.* **30** 6365-6388

[172] Zhou L B, Yuan T H, Li R D, Tang J Z, Wang M B and Mei F S 2018 Anisotropic mechanical behavior of biomedical Ti-13Nb-13Zr alloy manufactured by selective laser melting *J. Alloys Compd.* **762** 289-300

[173] Batalha R L, Batalha W C, Deng L, Gustmann T, Pauly S, Kiminami C S and Gargarella P 2020 Processing a biocompatible Ti-35Nb-7Zr-5Ta alloy by selective laser melting *J. Mater. Res.* **35** 1143-1153

[174] Ummethala R, Karamched P S, Rathinavelu S, Singh N, Aggarwal A, Sun K, Ivanov E, Kollo L, Okulov I and Eckert J 2020 Selective laser melting of high-strength, low-modulus Ti–35Nb–7Zr–5Ta alloy *Materialia.* **14** 100941

[175] Duan R, Li S, Cai B, Zhu W, Ren F and Attallah M M 2021 A high strength and low modulus metastable β Ti-12Mo-6Zr-2Fe alloy fabricated by laser powder bed fusion in-situ alloying *Addit. Manuf.* **37** 101708

[176] Huang H L, Li D, Chen C, Li R D, Zhang X Y, Liu S C and Zhou K C 2021 Selective laser melted near-beta titanium alloy Ti-5Al-5Mo-5V-1Cr-1Fe: Microstructure and mechanical properties *J. Cent. South Univ.* **28** 1601-1614

[177] Fan H Y and Yang S F 2020 Effects of direct aging on near-alpha Ti-6Al-2Sn-4Zr-2Mo (Ti-6242) titanium alloy fabricated by selective laser melting (SLM) *Materials Science and Engineering a-Structural Materials Properties Microstructure and Processing.* **788** 139533

[178] Carrozza A, Aversa A, Fino P and Lombardi M 2021 A study on the microstructure and mechanical properties of the Ti-6Al-2Sn-4Zr-6Mo alloy produced via Laser Powder Bed Fusion *J. Alloys Compd.* **870** 159329

[179] Zhang J and Singer R F 2002 Hot tearing of nickel-based superalloys during directional solidification *Acta Materialia.* **50** 1869-1879

[180] Rappaz M, Drezet J M and Gremaud M 1999 A new hot-tearing criterion *Metallurgical and Materials Transactions a-Physical Metallurgy and Materials Science.* **30** 449-455

[181] Hunt J 1979 The Metal Society, London Solidification and casting of metals **3** 275-278

[182] Xu J, Gruber H, Lin Peng R and Moverare J 2020 A Novel γ′ -Strengthened Nickel-Based Superalloy for Laser Powder Bed Fusion *Materials.* **13** 4930

[183] Griffiths S, Tabasi H G, Ivas T, Maeder X, De Luca A, Zweiacker K, Wróbel R, Jhabvala J, Logé R and Leinenbach C 2020 Combining alloy and process modification for micro-crack mitigation in an additively manufactured Ni-base superalloy *Addit. Manuf.* **36** 101443

[184] Aversa A, Marchese G, Saboori A, Bassini E, Manfredi D, Biamino S, Ugues D, Fino P and Lombardi M 2019 New Aluminum Alloys Specifically Designed for Laser Powder Bed Fusion: A Review *Materials.* **12** 1007

[185] Sun Z, Tan X, Wang C, Descoins M, Mangelinck D, Tor S B, Jägle E A, Zaefferer S and Raabe D 2021 Reducing hot tearing by grain boundary segregation engineering in additive manufacturing: example of an AlxCoCrFeNi high-entropy alloy *Acta Materialia.* **204** 116505

[186] Sweet L, Easton M A, Taylor J A, Grandfield J F, Davidson C J, Lu L, Couper M J and StJohn D H 2013 Hot Tear Susceptibility of Al-Mg-Si-Fe Alloys with Varying Iron Contents *Metallurgical and Materials Transactions A.* **44** 5396-5407

[187] Singh A, Ramakrishnan A, Baker D, Biswas A and Dinda G P 2017 Laser metal deposition of nickel coated Al 7050 alloy *Journal of Alloys and Compounds.* **719** 151-158

[188] Sun Z, Ma Y, Ponge D, Zaefferer S, Jägle E A, Gault B, Rollett A D and Raabe D 2022 Thermodynamics-guided alloy and process design for additive manufacturing *Nature Communications.* **13** 4361

[189] Thapliyal S, Agrawal P, Agrawal P, Nene S S, Mishra R S, McWilliams B A and Cho K C 2021 Segregation engineering of grain boundaries of a metastable Fe-Mn-Co-Cr-Si high entropy alloy with laser-powder bed fusion additive manufacturing *Acta Mater.* **219** 117271

[190] Zhang D, Qiu D, Gibson M A, Zheng Y, Fraser H L, StJohn D H and Easton M A 2019 Additive manufacturing of ultrafine-grained high-strength titanium alloys *Nature.* **576** 91-95

[191] Bermingham M J, McDonald S D, StJohn D H and Dargusch M S 2009 Beryllium as a grain refiner in titanium alloys *Journal of Alloys and Compounds.* **481** L20-L23

[192] Easton M A and StJohn D H 2001 A model of grain refinement incorporating alloy constitution and potency of heterogeneous nucleant particles *Acta Materialia.* **49** 1867-1878

[193] Tan Q, Yin Y, Prasad A, Li G, Zhu Q, StJohn D H and Zhang M-X 2022 Demonstrating the roles of solute and nucleant in grain refinement of additively manufactured aluminium alloys *Additive Manufacturing.* **49** 102516

[194] Guo Q, Qu M, Chuang C A, Xiong L, Nabaa A, Young Z A, Ren Y, Kenesei P, Zhang F and Chen L 2022 Phase transformation dynamics guided alloy development for additive manufacturing *Additive Manufacturing.* **59** 103068

[195] Wang Y M*et al* 2018 Additively manufactured hierarchical stainless steels with high strength and ductility *Nature Materials.* **17** 63-71

[196] Kürnsteiner P, Wilms M B, Weisheit A, Gault B, Jägle E A and Raabe D 2020 High-strength Damascus steel by additive manufacturing *Nature.* **582** 515-519

[197] Mereddy S, Bermingham M J, Kent D, Dehghan-Manshadi A, StJohn D H and Dargusch M S 2018 Trace Carbon Addition to Refine Microstructure and Enhance Properties of Additive-Manufactured Ti-6Al-4V *JOM.* **70** 1670-1676

[198] Gou J, Wang Z, Hu S, Shen J, Tian Y, Zhao G and Chen Y 2020 Effects of trace Nb addition on microstructure and properties of Ti–6Al–4V thin-wall structure prepared via cold metal transfer additive manufacturing *Journal of Alloys and Compounds.* **829** 154481

[199] Narayana P L, Lee S, Choi S-W, Li C-L, Park C H, Yeom J-T, Reddy N S and Hong J-K 2019 Microstructural response of β-stabilized Ti–6Al–4V manufactured by direct energy deposition *Journal of Alloys and Compounds.* **811** 152021

[200] Simonelli M, McCartney D G, Barriobero-Vila P, Aboulkhair N T, Tse Y Y, Clare A and Hague R 2020 The Influence of Iron in Minimizing the Microstructural Anisotropy of Ti-6Al-4V Produced by Laser Powder-Bed Fusion *Metallurgical and Materials Transactions A.* **51** 2444-2459

[201] Kendig K L and Miracle D B 2002 Strengthening mechanisms of an Al-Mg-Sc-Zr alloy *Acta Materialia.* **50** 4165-4175

[202] Spierings A B, Dawson K, Voegtlin M, Palm F and Uggowitzer P J 2016 Microstructure and mechanical properties of as-processed scandium-modified aluminium using selective laser melting *CIRP Annals.* **65** 213-216

[203] Jia Q, Rometsch P, Cao S, Zhang K, Huang A and Wu X 2018 Characterisation of AlScZr and AlErZr alloys processed by rapid laser melting *Scripta Materialia.* **151** 42-46

[204] Manca D R, Churyumov A Y, Pozdniakov A V, Prosviryakov A S, Ryabov D K, Krokhin A Y, Korolev V A and Daubarayte D K 2019 Microstructure and Properties of Novel Heat Resistant Al–Ce–Cu Alloy for Additive Manufacturing *Metals and Materials International.* **25** 633-640

[205] Manca D R, Churyumov A Y, Pozdniakov A V, Ryabov D K, Korolev V A and Daubarayte D K 2019 Novel heat-resistant Al-Si-Ni-Fe alloy manufactured by selective laser melting *Materials Letters.* **236** 676-679

[206] Croteau J R, Griffiths S, Rossell M D, Leinenbach C, Kenel C, Jansen V, Seidman D N, Dunand D C and Vo N Q 2018 Microstructure and mechanical properties of Al-Mg-Zr alloys processed by selective laser melting *Acta Materialia.* **153** 35-44

[207] Carroll B E, Palmer T A and Beese A M 2015 Anisotropic tensile behavior of Ti–6Al–4V components fabricated with directed energy deposition additive manufacturing *Acta Materialia.* **87** 309-320

[208] Zhang K, Tian X, Bermingham M, Rao J, Jia Q, Zhu Y, Wu X, Cao S and Huang A 2019 Effects of boron addition on microstructures and mechanical properties of Ti-6Al-4V manufactured by direct laser deposition *Materials & Design.* **184** 108191

[209] Sui S, Chew Y X, Weng F, Tan C L, Du Z L and Bi G J 2022 Study of the intrinsic mechanisms of nickel additive for grain refinement and strength enhancement of laser aided additively manufactured Ti-6Al-4V *Int. J. Extreme Manuf.* **4** 035102

[210] Yu W, Xiao Z, Zhang X, Sun Y, Xue P, Tan S, Wu Y and Zheng H 2022 Processing and characterization of crack-free 7075 aluminum alloys with elemental Zr modification by laser powder bed fusion *Materials Science in Additive Manufacturing.* **1** 4

[211] Zhang X H, Xiao Z, Yu W H, Chua C K, Zhu L H, Wang Z S, Xue P, Tan S, Wu Y L and Zheng H Y 2022 Influence of erbium addition on the defects of selective laser-melted 7075 aluminium alloy *Virtual Phys. Prototyping.* **17** 406-418

[212] Nie X, Zhang H, Zhu H, Hu Z, Ke L and Zeng X 2018 Effect of Zr content on formability, microstructure and mechanical properties of selective laser melted Zr modified Al-4.24 Cu-1.97 Mg-0.56 Mn alloys *Journal of Alloys Compounds.* **764** 977-986

[213] Sing S L, Kuo C N, Shih C T, Ho C C and Chua C K 2021 Perspectives of using machine learning in laser powder bed fusion for metal additive manufacturing *Virtual Phys. Prototyping.* **16** 372-386372

[214] Liu P, Huang H, Antonov S, Wen C, Xue D, Chen H, Li L, Feng Q, Omori T and Su Y 2020 Machine learning assisted design of γ'-strengthened Co-base superalloys with multi-performance optimization *npj Comput. Mater.* **6** 62

[215] Yong W, Zhang H T, Fu H D, Zhu Y L, He J and Xie J X 2022 Improving prediction accuracy of high-performance materials via modified machine learning strategy *Comput. Mater. Sci.* **204** 111181

[216] Wen C, Zhang Y, Wang C X, Xue D Z, Bai Y, Antonov S, Dai L H, Lookman T and Su Y J 2019 Machine learning assisted design of high entropy alloys with desired property *Acta Mater.* **170** 109-117

[217] Dreano A, Favre J, Desrayaud C, Chanin-Lambert P, Wimmer A and Zaeh M F 2022 Computational design of a crack-free aluminum alloy for additive manufacturing br *Addit. Manuf.* **55** 102876

[218] Du Y, Mukherjee T and DebRoy T 2021 Physics-informed machine learning and mechanistic modeling of additive manufacturing to reduce defects *Appl. Mater. Today.* **24** 101123

[219] Hu M W, Tan Q Y, Knibbe R, Wang S, Li X, Wu T Q, Jarin S and Zhang M X 2021 Prediction of Mechanical

Properties of Wrought Aluminium Alloys Using Feature Engineering Assisted Machine Learning Approach *Metallurgical and Materials Transactions a-Physical Metallurgy and Materials Science.* **52** 2873-2884

[220] Wang J, Xiao B and Liu Y 2020 Machine Learning Assisted High-Throughput Experiments Accelerates the Composition Design of Hard High-Entropy Alloy Co_xCr_yTi_zMo_uW_v *Materials China.* **39** 269-277

[221] Mondal B, Mukherjee T and DebRoy T 2022 Crack free metal printing using physics informed machine learning *Acta Mater.* **226** 117612

[222] Zhang H T, Fu H D, He X Q, Wang C S, Jiang L, Chen L Q and Xie J X 2020 Dramatically Enhanced Combination of Ultimate Tensile Strength and Electric Conductivity of Alloys via Machine Learning Screening *Acta Mater.* **200** 803-810

[223] Zhang H T, Fu H D, Zhu S C, Yong W and Xie J X 2021 Machine learning assisted composition effective design for precipitation strengthened copper alloys *Acta Mater.* **215** 117118

[224] Wang C S, Fu H D, Jiang L, Xue D Z and Xie J X 2019 A property-oriented design strategy for high performance copper alloys via machine learning *npj Comput. Mater.* **5** 87

[225] Jiang L, Wang C S, Fu H D, Shen J, Zhang Z H and Xie J X 2022 Discovery of aluminum alloys with ultra-strength and high-toughness via a property-oriented design strategy *Journal of Materials Science & Technology.* **98** 33-43

[226] Xue D Z, Balachandran P V, Hogden J, Theiler J, Xue D Q and Lookman T 2016 Accelerated search for materials with targeted properties by adaptive design *Nat. Commun.* **7** 11241

[227] Li S, Li S, Liu D R, Zou R and Yang Z Y 2022 Hardness prediction of high entropy alloys with machine learning and material descriptors selection by improved genetic algorithm *Comput. Mater. Sci.* **205** 111185

[228] Feng X M, Wang Z L, Jiang L, Zhao F and Zhang Z H 2023 Simultaneous enhancement in mechanical and corrosion properties of Al-Mg-Si alloys using machine learning *Journal of Materials Science & Technology.* **167** 1-13

[229] Chen Y Y, Wang H Z, Wu Y and Wang H W 2020 Predicting the Printability in Selective Laser Melting with a Supervised Machine Learning Method *Materials.* **13** 5063

[230] Liu Q, Wu H K, Paul M J, He P D, Peng Z X, Gludovatz B, Kruzic J J, Wang C H and Li X P 2020 Machine-learning assisted laser powder bed fusion process optimization for AlSi10Mg: New microstructure description indices and fracture mechanisms *Acta Mater.* **201** 316-328

[231] Lu C Y, Jia X D, Lee J and Shi J 2022 Knowledge transfer using Bayesian learning for predicting the process-property relationship of Inconel alloys obtained by laser powder bed fusion *Virtual Phys. Prototyping.* **17** 787-805

[232] Huang D J and Li H 2021 A machine learning guided investigation of quality repeatability in metal laser powder bed fusion additive manufacturing *Mater. Des.* **203** 109606

[233] Ozel T, Altay A, Kaftanoglu B, Leach R, Senin N and Donmez A 2020 Focus Variation Measurement and Prediction of Surface Texture Parameters Using Machine Learning in Laser Powder Bed Fusion *Journal of Manufacturing Science and Engineering-Transactions of the Asme.* **142** 011008

[234] Snow Z, Diehl B, Reutzel E W and Nassar A 2021 Toward in-situ flaw detection in laser powder bed fusion additive manufacturing through layerwise imagery and machine learning *J. Manuf. Syst.* **59** 12-26

[235] Ertay D S, Kamyab S, Vlasea M, Azimifar Z, Ma T, Rogalsky A D and Fieguth P 2021 Toward Sub-Surface Pore Prediction Capabilities for Laser Powder Bed Fusion Using Data Science *Journal of Manufacturing Science and Engineering-Transactions of the Asme.* **143** 071016

[236] Scime L and Beuth J 2018 A multi-scale convolutional neural network for autonomous anomaly detection and classification in a laser powder bed fusion additive manufacturing process *Addit. Manuf.* **24** 273-286

[237] Chen Y, Peng X, Kong L B, Dong G X, Remani A and Leach R 2021 Defect inspection technologies for additive manufacturing *Int. J. Extreme Manuf.* **3** 022002

[238] Mukherjee T, Wei H, De A and DebRoy T 2018 Heat and fluid flow in additive manufacturing—Part I: Modeling of powder bed fusion *Comput. Mater. Sci.* **150** 304-313

[239] Mukherjee T, Wei H, De A and DebRoy T 2018 Heat and fluid flow in additive manufacturing–Part II: Powder bed fusion of stainless steel, and titanium, nickel and aluminum base alloys *Comput. Mater. Sci.* **150** 369-380

[240] Schwendner K I, Banerjee R, Collins P C, Brice C A and Fraser H L 2001 Direct laser deposition of alloys from elemental powder blends *Scr. Mater.* **45** 1123-1129

[241] Grigoriev A, Polozov I, Sufiiarov V and Popovich A 2017 In-situ synthesis of Ti2AlNb-based intermetallic alloy by selective laser melting *Journal of Alloys and Compounds.* **704** 434-442